

# Electrochemically Induced Borate Allotropes for Expedite Charge Transfer in Lithium-Ion Batteries and Hydroxyl Ion Capture Activity in Flexible Pseudocapacitor

Kavibharathy Kasiviswanathan,<sup>[a]</sup> Kumaresan Lakshmanan,<sup>[a]</sup> Senthil Chenrayan,<sup>[b]</sup> Chang Woo Lee,<sup>[c]</sup> Baskaran Rangasamy,<sup>\*[d]</sup> and Kumaran Vediappan<sup>\*[a]</sup>

Despite lithium-ion battery (LIB) and supercapacitor materials have gone through numerous enhancements, achieving high energy density as well as power density together is still a dream for the industries. In this scenario, herein we report, boric acid coated  $\alpha$ -MnO<sub>2</sub> anode with 1288 mAh g<sup>-1</sup> at 0.1 C at the initial cycle and of an average discharge capacity of 570 mAh g<sup>-1</sup> at 0.1 C over 20 cycles, high-rate capability and 100% Coulombic efficiency after 60 cycles for LIB. The Li<sup>+</sup> diffusion coefficient estimated from GITT and EIS measurements reveals that the H<sub>3</sub>BO<sub>3</sub> coated  $\alpha$ -MnO<sub>2</sub> electrode has superior Li-ion kinetics ( $D_{Li^+} \sim 10^{-10}$  cm<sup>2</sup> s<sup>-1</sup>) than bare  $\alpha$ -MnO<sub>2</sub>. Coin cells with boric acid coated  $\alpha$ -MnO<sub>2</sub> electrode are able to power up red and blue

LEDs continuously for about 24–32 hours. The ex-situ investigations reveal an interesting self-assembled active electrode-electrolyte interfacial bridging Li<sub>4</sub>B<sub>2</sub>O<sub>5</sub> layer formation. This significant active layer allows free migration of lithium ions across interface that leads to good cyclability. In flexible supercapacitor, the boric acid coated  $\alpha$ -MnO<sub>2</sub> yields excellent cyclability over 500 cycles with specific capacitance of 35 F g<sup>-1</sup> at 1 A g<sup>-1</sup> and further 200 cycles at 30° acute angle with 21 F g<sup>-1</sup> at 1 A g<sup>-1</sup>. The research overthrows the significance of boric acid in conversion reactions for active interfacial bridging layer in LIB and hydroxyl ion capturing agent in flexible supercapacitor.

## Introduction

In the modern society, energy storage and conversion devices such as rechargeable lithium-ion batteries (LIBs) and supercapacitors (SCs) have received an enormous interest due to their respective high energy and power density.<sup>[1,2]</sup> In LIBs, despite various anode materials studied, achieving high capacity, and cyclic stability are the challenging tasks. On the other hand, attaining electrochemically stable symmetry electrodes for supercapacitors is a tedious process. In this scenario, the transition metal oxides (TMOs) have attracted a great attention and been promising alternative anode materials for

the rechargeable LIBs as well as symmetry electrodes for SCs.<sup>[3,4]</sup> TMO exhibits high theoretical capacity, safety, environmental benignity, natural abundance and low cost of raw materials.<sup>[5,6]</sup> In LIBs, various manganese-based oxides such as Mn<sub>3</sub>O<sub>4</sub>,<sup>[7]</sup> MnO,<sup>[8]</sup> Mn<sub>2</sub>O<sub>3</sub>,<sup>[9]</sup> and MnO<sub>2</sub><sup>[10]</sup> deliver a higher theoretical capacity of 936, 756, 1019 and 1232 mAh g<sup>-1</sup>, respectively,<sup>[11]</sup> based on the oxidation state of the manganese oxide. MnO<sub>2</sub> became highly attractive anode material for LIBs due to its superior theoretical capacity while compared to other transition metal oxides such as NiO<sub>2</sub>, CoO<sub>2</sub>, and CrO<sub>2</sub>. When compared to other metal oxides, MnO<sub>2</sub> is most stable with excellent physical and chemical properties under ambient conditions.<sup>[12,13]</sup> Basically, MnO<sub>2</sub> is found in five different phases, e.g.,  $\alpha$ -MnO<sub>2</sub>,  $\beta$ -MnO<sub>2</sub>,  $\gamma$ -MnO<sub>2</sub>,  $\delta$ -MnO<sub>2</sub> and  $\epsilon$ -MnO<sub>2</sub>, among which  $\alpha$ -MnO<sub>2</sub> is being used as a negative electrode for the fabrication of rechargeable LIBs, because of its high theoretical capacity (for 1 ion = 308.3 mAh g<sup>-1</sup>, 4 ion = 1232 mAh g<sup>-1</sup>).<sup>[14,15]</sup> Alfaruqi et al. reported a cryptomelane-type  $\alpha$ -MnO<sub>2</sub> [2×2] with unique tunnel structure which exhibits reversible redox kinetics of lithium ions.<sup>[16]</sup> The  $\alpha$ -MnO<sub>2</sub> electrode has been widely reported as an anode material to store various ions such as (Li<sup>+</sup>, Na<sup>+</sup> and Mg<sup>2+</sup>).<sup>[17]</sup>

TMO electrodes delivered high capacitance in pseudocapacitors, similarly as in LIBs.<sup>[18]</sup> However, achieving high theoretical capacitance and long stability in practical is a challenging task both in LIBs and SCs due to the prevailing issues such as huge volume expansion, particle pulverization during repeated cycling, loss of electrical contact among the electrode particles, poor electronic conductivity and passivation layer formation.<sup>[19,20]</sup> In order to get rid of these critical issues, MnO<sub>2</sub> with various geometrical morphologies such as nanorods,

[a] K. Kasiviswanathan, K. Lakshmanan, Dr. K. Vediappan  
Electrochemical Energy Storage and Conversion Laboratory (EESCL)

Department of Chemistry, Faculty of Engineering and Technology  
SRM Institute of Science and Technology  
Kattankulathur-603 203, Tamil Nadu, India  
E-mail: kumaranv@srmiss.edu.in

[b] Dr. S. Chenrayan  
Department of Energy Engineering  
Gyeongsang National University  
Jinju-si, Gyeongnam, 52725, South Korea

[c] Prof. C. Woo Lee  
Department of Chemical Engineering (integrated Engineering) & Center for the SMART Energy Platform  
College of Engineering  
Kyung Hee University  
1732 Deogyoeng-daero, Gihueng, Yongin, Gyeonggi 17104, South Korea

[d] Prof. B. Rangasamy  
Department of Physics, School of Mathematics and Natural Sciences  
The Copperbelt University  
P.O.Box 21692, Riverside, Jambo Drive, Kitwe 10101, Zambia  
E-mail: baskaran.rangasamy@cbu.ac.zm

 Supporting information for this article is available on the WWW under  
<https://doi.org/10.1002/batt.202200449>

nanowires, nanoflakes, nanosheets and nanotubes have been studied so far, however the results are not encouraging. Although different nano-architectures received great attention due to huge surface area, minimized grain boundary resistance and enhanced Li-ion diffusion rate, the surface of the electrodes are prone to high reactivity with the electrolytes that leads to rapid development of passive solid electrolyte interfacial (SEI) layer.<sup>[21]</sup>

In this work, an innovative approach of synthesizing  $\alpha\text{-MnO}_2$  nanorods followed by surface coating with boric acid ( $\text{H}_3\text{BO}_3$ ) has been introduced which is predicted to wrap the nanorods and also acts as an ion transport medium among the electrode particles. Upon cycling the lithium-ion cell, it's expected that the upper surface boric acid could form an active SEI layer between electrode-electrolyte with faster interfacial ion mobility during redox reactions. The significance of self-driven active SEI layer in prolonged powering blue and red LEDs and electrochemical performance of LIBs have been discussed. Another interesting impact of this article is a novel design engineering of flexible transparent supercapacitor (FTSC) device with the boric acid coated  $\alpha\text{-MnO}_2$ . The structural, high resolution transmission electron microscope (HRTEM), selected area electron diffraction (SAED), and elemental mapping have been carried out on bare and boric acid coated  $\alpha\text{-MnO}_2$  powder sample in order to confirm the nature of compound formation. The comparison of electrochemical performances of both bare and boric acid coated  $\alpha\text{-MnO}_2$  electrodes in LIB and outperformed  $\text{H}_3\text{BO}_3$  coated  $\alpha\text{-MnO}_2$  in FTSC device has been evaluated with cyclic voltammetry, galvanostatic charge-discharge and electrochemical impedance spectroscopy (EIS) measurements. The galvanostatic intermittent titration (GITT) measurements along with EIS technique have been used to estimate the  $\text{Li}^+$  ion diffusion coefficients of the bare and coated  $\alpha\text{-MnO}_2$  electrodes. The self-driven in-situ formation of  $\text{Li}_4\text{B}_2\text{O}_5$  as an active SEI layer in LIB by the facile reaction kinetics of boric acid with lithium has been demonstrated by an ex-situ post-investigation of redox cycled  $\text{H}_3\text{BO}_3$  coated  $\alpha\text{-MnO}_2$  electrodes with X-ray diffraction (XRD), cross-section HRSEM and FTIR analyses. The role of boric acid in terms of electrochemical efficiency by nanorod surface protection, electrode surface kinetics, and electrical contact among the particles has been interpreted.

## Results and Discussion

The  $\alpha\text{-MnO}_2$  nanorods has been synthesized by Pechini method and then an elegant boric acid coating on  $\alpha\text{-MnO}_2$  is achieved through physical method at 650 °C as illustrated in Scheme S1 (Supporting Information). As prepared and boric acid coated  $\alpha\text{-MnO}_2$  are taken for electrode fabrication in a usual method with carbon black and PVDF on copper foil. The  $\alpha\text{-MnO}_2$  based working electrodes are used to construct lithium-ion coin cell in an argon filled glove box and then electrochemical, subsequent ex-situ measurements are carried out. The outperformed  $\text{H}_3\text{BO}_3$  coated  $\alpha\text{-MnO}_2$  electrodes are used to construct FTSC device and electrochemical measure-

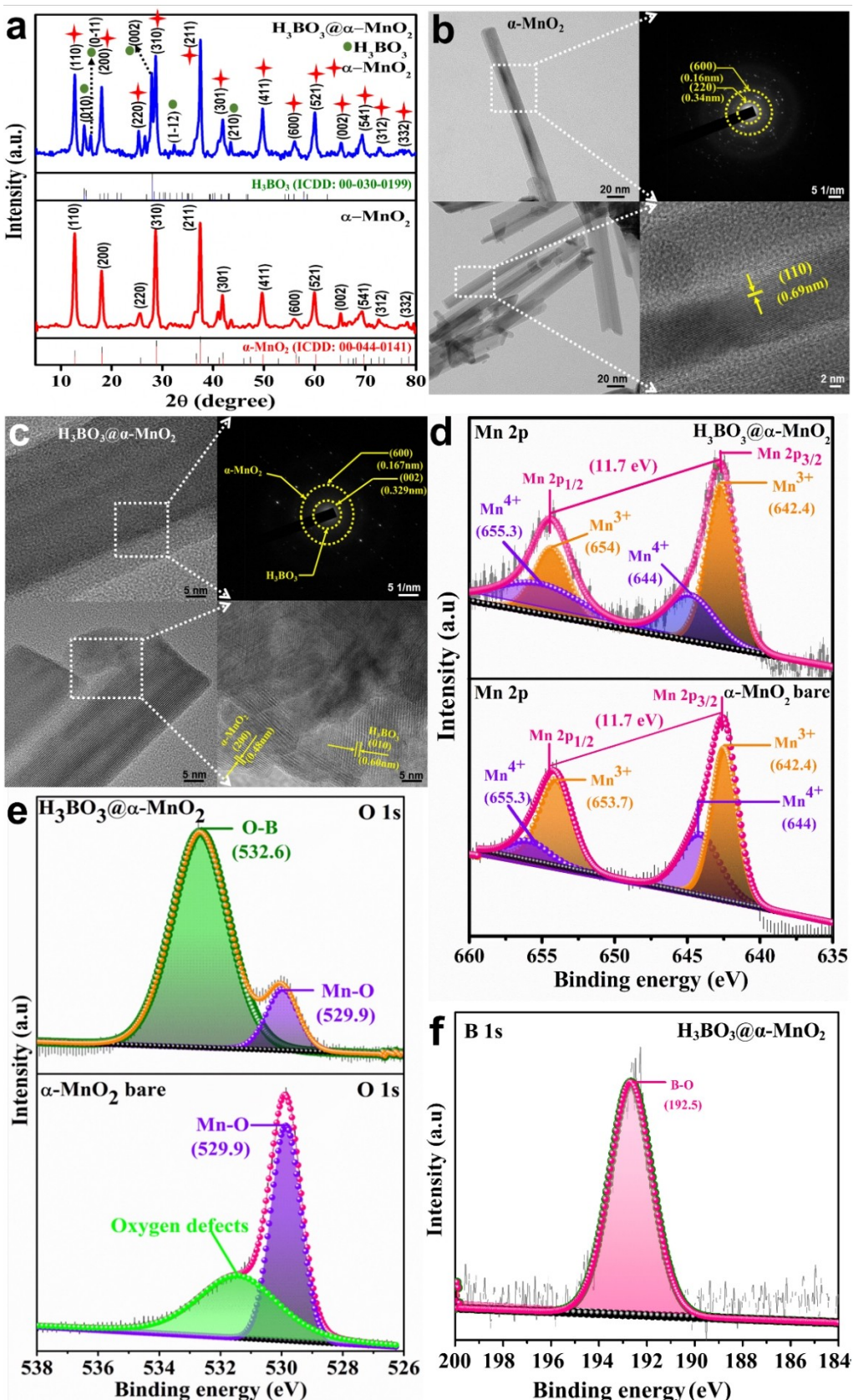
ments at flat and 30° bending angle are performed as shown in the digital images (Figure S1, Supporting Information). The precursor material details, synthesis of  $\alpha\text{-MnO}_2$  nanorods, boric acid coating procedures, electrode fabrication followed by LIB and FTSC constructions, instrumental details for physical, electrochemical and ex-situ investigations are elaborately discussed under Experimental Section in the Supporting Information.

Figure 1(a) shows XRD pattern comparison of as-synthesized bare  $\alpha\text{-MnO}_2$  and  $\text{H}_3\text{BO}_3@\alpha\text{-MnO}_2$ . The existence of sharp diffraction peaks ( $\theta$ ) at 12.714°, 18.011°, 25.586°, 28.673°, 37.460°, 41.844°, 49.670°, 56.019°, 59.991°, 65.221°, 69.098°, 72.646° and 78.422° in both XRD patterns are corresponding to (110), (200), (220), (310), (211), (301), (411), (600), (521), (002), (541), (312) and (332) crystal planes, which indicate the formation of pure tetragonal phase of pristine  $\alpha\text{-MnO}_2$  (ICDD: 00-044-0141).<sup>[22]</sup> In the boric acid coated sample, the presence of  $\text{H}_3\text{BO}_3$  is confirmed by the peaks ( $\theta$ ) at 14.63°, 15.864°, 28.0°, 32.40° and 43.30° corresponding to (010), (0-11), (002), (1-12) and (210) crystal planes (ICDD: 00-030-0199).<sup>[23]</sup> The grain sizes are estimated by using Debye-Scherrer's relation,<sup>[24]</sup> which indicates 15.63 nm and 21.1 nm for bare and  $\text{H}_3\text{BO}_3$  coated  $\alpha\text{-MnO}_2$ , respectively.

Figure S2(a-d), in Supporting Information, shows HRSEM images of bare and  $\text{H}_3\text{BO}_3$  coated  $\alpha\text{-MnO}_2$  nanorods which reveal an average length of ~350–450 nm while the diameters are of ~20–25 nm and ~30–35 nm, respectively. Figure S3(a-c) shows nanorod morphology of  $\alpha\text{-MnO}_2$ , and its elemental mapping indicates the presence of evenly distributed manganese, and oxygen in  $\alpha\text{-MnO}_2$  which implies single phase formation as evidenced in XRD. Figure S4(a-d) indicates uniform coating of boric acid on the  $\alpha\text{-MnO}_2$  nanorod surface and its elemental mapping illustrates orderly distribution of manganese, oxygen and boron in  $\text{H}_3\text{BO}_3@\alpha\text{-MnO}_2$ .

Figure 1(b) indicates formation of  $\alpha\text{-MnO}_2$  nanorod with a length of 450 nm and uniform diameter 20 nm whereas in  $\text{H}_3\text{BO}_3@\alpha\text{-MnO}_2$ , diameter of inner nanorod is 22 nm wrapped by a thin layer of boric acid coating with 5–6 nm. The SAED pattern corresponding to the marked regions indicating (220), (600) and (110) planes with an interplanar distances  $d = 0.34$  nm, 0.16 nm, and 0.69 nm of  $\alpha\text{-MnO}_2$ , respectively. Figure 1(c) shows the SAED pattern of  $\text{H}_3\text{BO}_3@\alpha\text{-MnO}_2$  that clearly indicates dark spots that confirms the formation of two different polycrystalline structures corresponding to (002) plane of boric acid and (600) plane of  $\alpha\text{-MnO}_2$  nanorods with interplanar distances  $d = 0.329$  and 0.167 nm, respectively. As indicated in the SAED pattern, the outer set of dark spot belongs to the formation of  $\alpha\text{-MnO}_2$  nanorod and the other set of inner dark spots indicating the formation of  $\text{H}_3\text{BO}_3$ . Figure 1(c) indicates lattice fringes with an interplanar distance of  $d = 0.60$  nm corresponding to (010) plane of  $\text{H}_3\text{BO}_3$  and that of  $d = 0.48$  nm indexed to (200) plane of  $\alpha\text{-MnO}_2$ .

The surface chemical state of bare and  $\text{H}_3\text{BO}_3$  coated  $\alpha\text{-MnO}_2$  is investigated by XPS analysis to clarify the oxidation state of the components. The XPS survey spectra of bare and  $\text{H}_3\text{BO}_3$  coated  $\alpha\text{-MnO}_2$  are given in Figure S5(a and b) indicates the presence of Mn, O and B elements corresponding to the

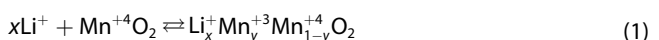


**Figure 1.** a) XRD pattern of bare and boric acid coated  $\alpha\text{-MnO}_2$ . b and c) HRTEM morphologies and SAED pattern of bare  $\alpha\text{-MnO}_2$  and  $\text{H}_3\text{BO}_3@\alpha\text{-MnO}_2$  nanorods. XPS spectra of bare and  $\text{H}_3\text{BO}_3$  coated  $\alpha\text{-MnO}_2$  in the energy range of d) Mn 2p, e) O 1s and f) B 1s signals.

respective samples in the binding energy range of 0–1400 eV. Figure 1(d) shows XPS spectra of bare and  $H_3BO_3$  coated  $\alpha$ - $MnO_2$  in the energy range of Mn 2p which depicts Mn 2p<sub>3/2</sub> and Mn 2p<sub>1/2</sub> signals at the binding energies of 642.2 and 654.1 eV, respectively with an energy separation of 11.7 eV. The signals of Mn are deconvoluted into a doublet of each signals Mn 2p<sub>3/2</sub> and Mn 2p<sub>1/2</sub> that represent a mixed valence state Mn<sup>3+</sup> and Mn<sup>4+</sup> of manganese.<sup>[25]</sup> These two oxidation states Mn<sup>3+</sup> and Mn<sup>4+</sup> of Mn 2p<sub>3/2</sub> appear at binding energy of 642.4, 644 eV and that of Mn 2p<sub>1/2</sub> at 653.7–654 eV and 655.3 eV respectively, which is an indication for the existence of oxygen vacancies on the surface of  $\alpha$ - $MnO_2$  in both the samples. The O 1s spectrum of  $\alpha$ - $MnO_2$  is shown in Figure 1(e) indicates a peak centered at 529.9 eV which is attributed to the binding energy of Mn–O bond<sup>[26]</sup> and an oxygen defect peak centered at 531.2 eV.<sup>[27]</sup> The appearance of oxygen defect peak in  $\alpha$ - $MnO_2$  might be due to the mild lattice disorder and dislocations as illustrated for Figure S6. The O 1s spectrum of  $H_3BO_3@\alpha$ - $MnO_2$  (Figure 1e) indicates two components at 532.6 and 529.9 eV corresponding to O–B<sup>[28]</sup> and Mn–O<sup>[29]</sup> bonds respectively. As shown in Figure 1(f), B 1s spectrum indicates a peak at 192.5 eV which is corresponding to B–O bond formation in  $H_3BO_3@\alpha$ - $MnO_2$ .<sup>[28]</sup>

Figure 2(a and b) shows the cyclic voltammogram (CV) results exhibiting kinetics of Li<sup>+</sup> insertion/de-insertion of  $\alpha$ - $MnO_2$  and  $H_3BO_3@\alpha$ - $MnO_2$  electrode materials. The first negative scans show slight humps at 2.4, 1.5 V in  $\alpha$ - $MnO_2$  bare and that of  $H_3BO_3@\alpha$ - $MnO_2$  at 2.42, 1.86, 1.56 and 0.75 V, which are attributed to the SEI layer formation on the surface of the electrodes in both the samples.<sup>[30]</sup> The surface adsorbed oxygen and oxygen released due to surface Mn dissolution gets reduced with lithium-ion. This leads to the formation of intermetallic irreversible Li<sub>2</sub>O compound as SEI layer on the surface of the electrode, which is reflected as irreversible capacity in the subsequent cycles of  $\alpha$ - $MnO_2$  electrode.

Whereas in  $H_3BO_3@\alpha$ - $MnO_2$  electrode, the Mn dissolution is protected by boric acid coating in which the BO<sup>3-</sup> is expected to reduce with lithium-ion causing Li–B–O based SEI layer. This phenomenon is evidenced by the appearance of slight peaks at 1.86 and 0.75 V (which may be due to Li–B–O layer formation), and the decreased humpy peaks at 2.4 and 1.56 V (which indicates negligible surface Mn dissolution and hence a small amount of Li<sub>2</sub>O formation is expected only due to surface adsorbed oxygen of the electrode). In addition, a significant strong cathodic peak is observed at 0.2 and 0.08 V in bare and  $H_3BO_3$  coated  $\alpha$ - $MnO_2$ , respectively indicates the reduction of Mn<sup>4+</sup> to Mn<sup>3+</sup>. The electrochemical reaction involved during the charge/discharge processes are exhibited by Equation (1),<sup>[31]</sup>



Whereas during the anodic processes of the first cycle in both the samples, an oxidation peak observed at 1.2–1.23 V confirms the oxidation of Mn<sup>3+</sup> to Mn<sup>4+</sup>. It's interesting to note that the cathodic peak position is widely shifted from 0.2 to 0.3 V and 0.08 to 0.36 V, while the anodic peaks remain closer in the bare and coated  $\alpha$ - $MnO_2$ , respectively in the subsequent

cycles. It might be explained by the electrochemical alternation of  $MnO_2$  and structural reconstruction according to the Li<sup>+</sup>/Li redox reactions. The redox peaks are well overlapped with one another without abrupt peak shift from the second cycle onwards, which reveals excellent electrochemical reversibility and structural stability of both  $\alpha$ - $MnO_2$  nanorods. A comparative analysis at 5<sup>th</sup> cycle (Figure S7, Supporting Information) indicates a single pair of redox peaks, and reveals the occurrence of Li<sup>+</sup>/Li redox reaction through a single transition stage in both the electrodes. Enhanced electrochemical performance is observed in  $H_3BO_3@\alpha$ - $MnO_2$  electrode, which might be due to the boric acid coating that prevents direct contact of electrodes with electrolyte and hence the electrode deterioration rate is much reduced.

Figure 2(c and d) depicts the galvanostatic charge/discharge profile of  $\alpha$ - $MnO_2$  nanorods for 20 cycles at a current rate of 0.1 C in the potential range between 0.1 to 3.0 V vs. Li<sup>+</sup>/Li. The initial discharge capacity of  $\alpha$ - $MnO_2$  nanorod is 953.6 mAh g<sup>-1</sup> and that of  $H_3BO_3@\alpha$ - $MnO_2$  is 1288 mAh g<sup>-1</sup> with a discharge plateau at 0.2 and 0.5 V, respectively. The second cycle of bare  $\alpha$ - $MnO_2$  delivers a discharge capacity of 298.9 mAh g<sup>-1</sup> which is almost close to the theoretical capacity (308.3 mAh g<sup>-1</sup>) of  $\alpha$ - $MnO_2$  meant for one Li<sup>+</sup>-ion intercalation.<sup>[32]</sup> The second cycle in boric acid coated  $\alpha$ - $MnO_2$  displays a discharge capacity of 619 mAh g<sup>-1</sup>. This initial rapid decrease in discharge capacity of bare  $\alpha$ - $MnO_2$  might be due to the amount of lithium spent with surface functionalized oxygen in  $\alpha$ - $MnO_2$  nanorods towards the formation of irreversible Li<sub>2</sub>O passive SEI layer on the surface of the electrode and that of Li–B–O active SEI layer formation in  $H_3BO_3@\alpha$ - $MnO_2$ . In general, the  $\alpha$ - $MnO_2$  nanorod has a large surface area and nanorod architecture, which leads to a columnar lithium storage and exhibits an initial high value of discharge capacity in both the electrodes. Upon further cycles, in both bare and coated  $\alpha$ - $MnO_2$  electrodes, the specific discharge capacities are gradually decreased to 181 and 286 mAh g<sup>-1</sup>, respectively at 20<sup>th</sup> cycle. In the case of  $H_3BO_3$  coated  $\alpha$ - $MnO_2$  nanorod, a relatively larger discharge capacity is observed, which infers significant role of boric acid in preventing the surface of nanorods from direct exposure to the electrolyte components in order to avoid unwanted reactions.

Figure 2(e and f) depicts the charge-discharge profile for selected cycles of  $\alpha$ - $MnO_2$  bare and  $H_3BO_3@\alpha$ - $MnO_2$  electrodes performed at a constant current rate of 1 C. The  $\alpha$ - $MnO_2$  bare electrode delivers the initial discharge capacity of 707 mAh g<sup>-1</sup> and exhibits two discharge sloppy plateaus at around 0.35 and 0.8 V. Whereas, the  $H_3BO_3@\alpha$ - $MnO_2$  electrode delivers the initial discharge capacity of 754 mAh g<sup>-1</sup> with plateaus at 0.35 and 0.8 V as that of bare  $\alpha$ - $MnO_2$  sample. Further cycles on these electrodes reveal only one cathodic plateau at 0.5 V along with an anodic peak at 1.2 V, corresponding to redox reactions. In both electrodes, there is enough time for electrochemical alteration to occur due to the slow kinetics at 0.1 C rate so that the discharge capacity reveals relatively higher values than the kinetics at 1 C rate. On further cycles of redox reactions, the specific discharge capacity of the  $\alpha$ - $MnO_2$  bare electrode gradually fades to 66 mAh g<sup>-1</sup> at 100<sup>th</sup> cycle, while

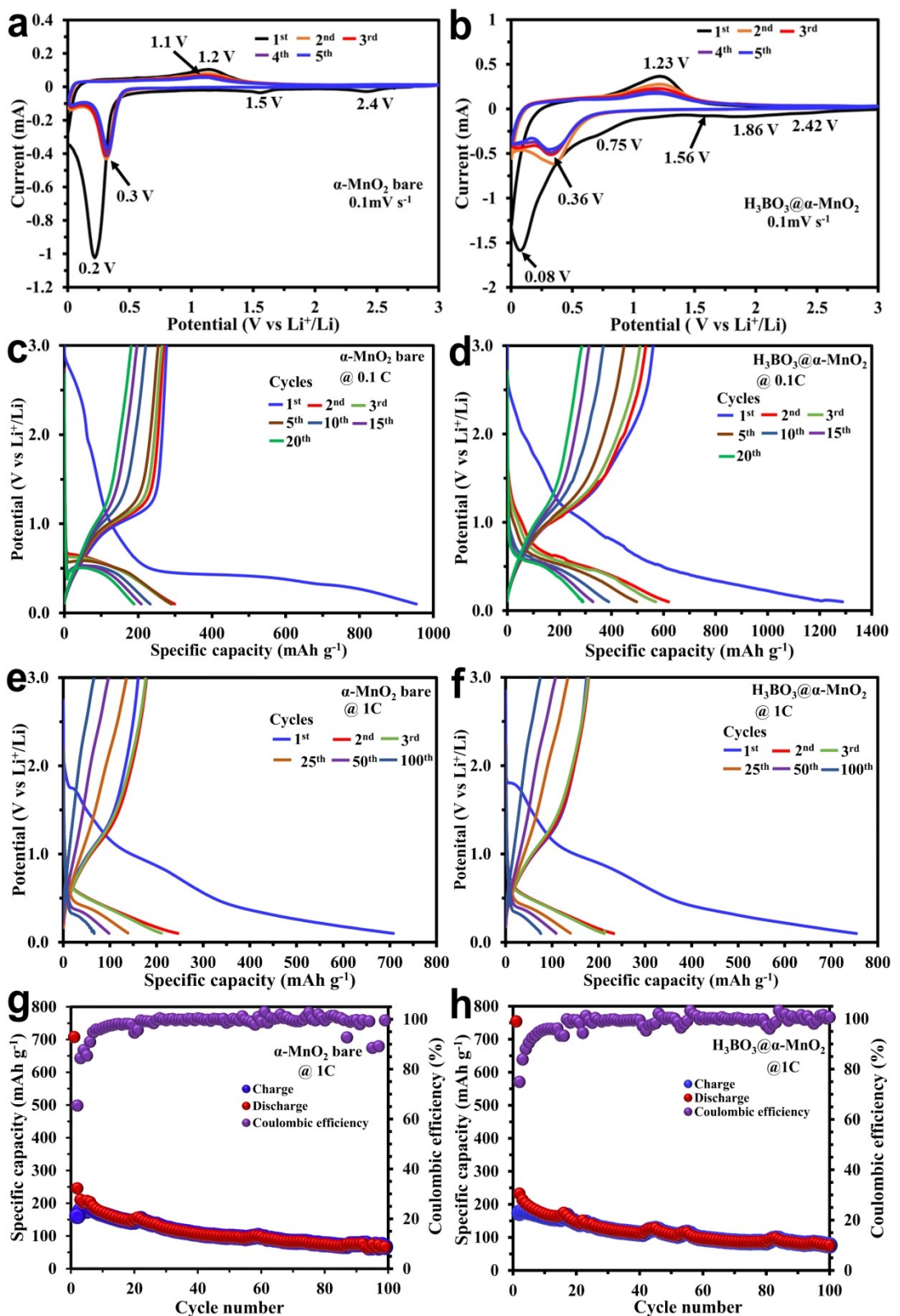


**Figure 2.** CV curves for initial five cycles of a)  $\alpha\text{-MnO}_2$  bare and b)  $\text{H}_3\text{BO}_3@\alpha\text{-MnO}_2$  vs.  $\text{Li}^+/\text{Li}$  at  $0.1 \text{ mV s}^{-1}$ . Galvanostatic charge-discharge curves of LIB with c)  $\alpha\text{-MnO}_2$  bare and d)  $\text{H}_3\text{BO}_3@\alpha\text{-MnO}_2$  vs.  $\text{Li}^+/\text{Li}$  at  $0.1 \text{ C}$ . Charge-discharge profile of LIB with e)  $\alpha\text{-MnO}_2$  bare and f)  $\text{H}_3\text{BO}_3@\alpha\text{-MnO}_2$  vs.  $\text{Li}^+/\text{Li}$  at  $1 \text{ C}$ . Cyclic performance of LIB with g)  $\alpha\text{-MnO}_2$  bare and h)  $\text{H}_3\text{BO}_3@\alpha\text{-MnO}_2$  versus  $\text{Li}^+/\text{Li}$  up to 100 cycles at  $1 \text{ C}$ .

that of  $76 \text{ mAh g}^{-1}$  in the case of  $\text{H}_3\text{BO}_3@\alpha\text{-MnO}_2$ . Figure 2(g and h) shows the specific capacity and Coulombic efficiency versus number of cycles of both the electrodes for 100 cycles at 1 C rate. Both the bare and coated electrodes exhibit rapid decrease of discharge capacity to 245 and  $232 \text{ mAh g}^{-1}$  in the second cycle with just a 63%–67.5% Coulombic efficiency. As discussed earlier, a large amount of lithium-ion is spent for the SEI layer formation in both electrodes, which leads to the huge irreversible capacity of 37%–33%. Upon further cycling, the discharge capacity gradually decreases to  $66 \text{ mAh g}^{-1}$  at 80<sup>th</sup> cycle in bare and similarly to  $\sim 76 \text{ mAh g}^{-1}$  at 60<sup>th</sup> cycle in  $\text{H}_3\text{BO}_3$  coated  $\alpha\text{-MnO}_2$  electrode. However, it's interesting to note that the further cycles on both electrodes indicate very stable discharge capacity (i.e., 66 and  $76 \text{ mAh g}^{-1}$ , respectively) up to 100<sup>th</sup> cycle with 100% excellent Coulombic efficiency. The gradual capacity fading in both  $\alpha\text{-MnO}_2$  and  $\text{H}_3\text{BO}_3@\alpha\text{-MnO}_2$  electrodes from 2<sup>nd</sup> cycle onwards might be due to the intermetallic compound formation such as  $\text{Li}_2\text{CO}_3$  and  $\text{Li}_2\text{O}$ , caused by lithium-ion reactions with free radicals of decomposed electrolyte components. While comparing both electrodes, the boric acid coated sample attains relatively high stability from 60<sup>th</sup> cycle onwards with better discharge capacity of  $76 \text{ mAh g}^{-1}$  until 100<sup>th</sup> cycle since coating prevents rupture of electrode and unwanted reaction of electrolyte components with active electrode. However, the real discharge capacity might be much higher than the observed discharge capacity of the  $\text{H}_3\text{BO}_3@\alpha\text{-MnO}_2$  electrode if the weight of inseparable redox inactive  $\text{H}_3\text{BO}_3$  is excluded from the total weight. When  $\text{H}_3\text{BO}_3$  coated on the surface of the  $\alpha\text{-MnO}_2$  metal oxide nanorods at 650 °C, an enhancement in the periodicity of the lattice (*d*-spacing) parameter and increasing relative crystallinity nature of the  $\alpha\text{-MnO}_2$  nanoparticles is observed as evidenced from XRD and HRTEM-SAED analyses. The high surface area and columnar structure of the nanorod helps to store more lithium-ions while the boric acid coating protects the  $\alpha\text{-MnO}_2$  nanorods from decomposed electrolyte constituents. In addition, a feasible pathway of lithium-ion migration through boric acid might be produced by electrochemical alteration which could also be the reason for higher charge/discharge capacity in boric acid coated electrode. A detailed literature survey (Table S1) on comparison of discharge capacity of  $\text{MnO}_2$  based electrodes show a relatively good performance of presently studied bare and  $\text{H}_3\text{BO}_3$  coated  $\alpha\text{-MnO}_2$  electrodes. The C-rate performance of  $\alpha\text{-MnO}_2$  bare and  $\text{H}_3\text{BO}_3@\alpha\text{-MnO}_2$  electrodes versus  $\text{Li}^+/\text{Li}$  at various current densities (Figure 3a and b) exhibits a descending step like behavior with increase of current densities. The  $\alpha\text{-MnO}_2$  bare electrode delivers discharge capacity of  $1098 \text{ mAh g}^{-1}$  at 0.1 C which drops down to  $98 \text{ mAh g}^{-1}$  at 2 C rate while that of  $971 \text{ mAh g}^{-1}$  at 0.1 C steps down to  $170 \text{ mAh g}^{-1}$  at 2 C in  $\text{H}_3\text{BO}_3@\alpha\text{-MnO}_2$  electrode. However, the discharge capacity exhibits an immediate step up of  $\sim 260\text{--}270 \text{ mAh g}^{-1}$  when the C-rate is suddenly decreased to 0.1 C rate in both the electrodes which might be due to the restricted lithium-ion redox at higher C-rate. The results reveal that both the coated and uncoated  $\alpha\text{-MnO}_2$  electrodes exhibit tolerance towards lithium redox kinetics even at high C-rate and capable to regain the charge/discharge capacities when

the C-rate is lowered. When both the electrodes are compared, the boric acid coated sample exhibits relatively better C-rate capability than the  $\alpha\text{-MnO}_2$  nanorods.

The nanorod formation provides high tensile strength, structural integrity and electrochemical stability to the electrode which enhances the diffusion kinetics for electronic and ionic transport.<sup>[33,34]</sup> The boric acid coated  $\alpha\text{-MnO}_2$  nanorod is highly ion conductive and possess well-ordered nanostructure that leads the  $\text{H}_3\text{BO}_3@\alpha\text{-MnO}_2$  nanorod electrode towards good reversibility. The  $\text{Li}^+$  ion diffusion coefficient obtained from GITT measurement (Figure S8) for bare and coated  $\alpha\text{-MnO}_2$  electrodes indicates  $D_{\text{Li}^+} = 7.13 \times 10^{-11} \text{ cm}^2 \text{ s}^{-1}$  and  $D_{\text{Li}^+} = 1.041 \times 10^{-10} \text{ cm}^2 \text{ s}^{-1}$ , respectively. The lithium-ion diffusion coefficient of  $\text{H}_3\text{BO}_3@\alpha\text{-MnO}_2$  electrodes show higher values than that of  $\alpha\text{-MnO}_2$  bare electrode which is in concurrence with the electrochemical performance.

Figure 3(c and d) depicts the electrochemical impedance spectroscopy (EIS) of Li-ion coin cell with bare and  $\text{H}_3\text{BO}_3$  coated  $\alpha\text{-MnO}_2$  nanorod electrodes before and after 100 cycles charge/discharge. The impedance spectra depict a low frequency spike, Warburg region and a high frequency depressed semicircle. The formation of depressed semi-circle in the high frequency region is related to the nature of electrode, surface inhomogeneity and surface roughness of the electrode material that causes frequency dispersion during measurement. The region-I observed in the impedance spectra indicates a solution resistance ( $R_s$ ) emerged by the electrolyte used in the system. In the high frequency region-II, a semicircle is observed for both before and after cycling indicates a charge transfer resistance ( $R_{ct}$ ) attributed to the ion transport in the electrolyte and electrode-electrolyte interface. The lithium-ion cell performance could be better when the  $R_{ct}$  value is smaller. The charge transfer resistance in the  $\alpha\text{-MnO}_2$  based coin cell before cycle indicates  $7.5 \Omega$  that increases to  $15 \Omega$  after hundred cycles, which might be due to the combined effect of electrolyte degradation followed by a passive SEI layer formation at the electrolyte-electrode interface. However, this increment in charge transfer resistance is not abrupt which is very well reflected in the charge/discharge profile in terms of better electrochemical stability even after 80 cycles. The charge transfer resistance ( $R_{ct}$ ) of Li-ion cell with  $\text{H}_3\text{BO}_3@\alpha\text{-MnO}_2$  electrode before cycling is found to be  $11 \Omega$  that is slightly higher than that of Li-ion cell with bare  $\alpha\text{-MnO}_2$  which might be due to the boric acid coating on the  $\alpha\text{-MnO}_2$  nanorods. However, it's interesting to note that the charge transfer resistance ( $R_{ct}$ ) of lithium-ion cell with  $\text{H}_3\text{BO}_3@\alpha\text{-MnO}_2$  decreases to  $8.5 \Omega$  after 100 cycles while compared to that of before cycling leads to the thinking that there might be an active Li-B–O SEI layer formed at the electrode-electrolyte interface. The  $\text{Li}^+$  ion diffusion coefficient evaluated by using impedance data (Figure S9) for the bare and coated  $\alpha\text{-MnO}_2$  electrodes before and after cycling reveals that the  $\text{H}_3\text{BO}_3@\alpha\text{-MnO}_2$  electrode has superior lithium-ion diffusion kinetics of  $D_{\text{Li}^+} = 7.5 \times 10^{-9} \text{ cm}^2 \text{ s}^{-1}$  after cycling as shown in Table S2.

It's supposed that the active SEI layer might have formed by consuming the electrode top layer boric acid and lithium-

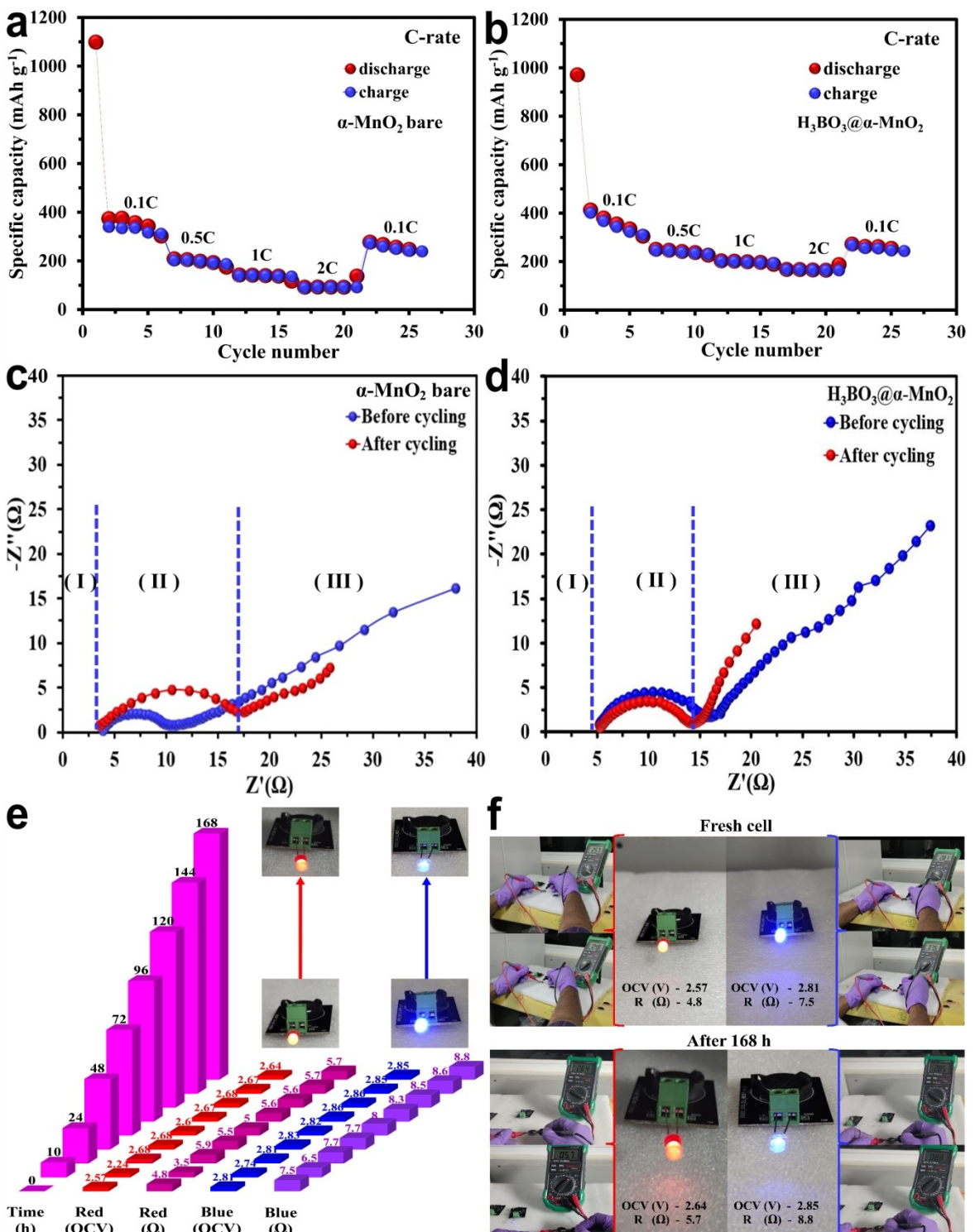


**Figure 3.** C-rate performance of LIB with a)  $\alpha\text{-MnO}_2$  bare and b)  $\text{H}_3\text{BO}_3@\alpha\text{-MnO}_2$  electrodes vs.  $\text{Li}^+/\text{Li}$  at different current densities. Nyquist plot of lithium-ion cell with c)  $\alpha\text{-MnO}_2$  bare and d)  $\text{H}_3\text{BO}_3@\alpha\text{-MnO}_2$  electrodes before and after 100 cycles. e) Variation of OCV and resistance during self-discharge of the LIB coin cells with  $\text{H}_3\text{BO}_3@\alpha\text{-MnO}_2$  electrode by intermittent powering of blue and red light-emitting diode (LEDs) tested for a week. f) Digital image of CR2032 coin cells powering red and blue LED with fresh cell and after 168 h of self-discharge.

ion reactions which enables facile charge transfer at the electrode-electrolyte interface and decreases the internal resistance of the system. In order to confirm existence of an

active SEI layer, detailed ex-situ investigations have been performed on the redox cycled electrodes. The notable decrease in the charge-transfer resistance after 100 cycles is in

concurrence with the 100% coulombic efficiency observed significantly for 60–100 cycle regions in the charge/discharge profile. The EIS results reveal that the boric acid plays a major role to enhance the ionic transport, electrochemical stability and evidenced an alleviation of large volumetric changes during the lithiation and de-lithiation process in to the  $\text{H}_3\text{BO}_3@\alpha\text{-MnO}_2$  nanorod. In both the electrodes, the low frequency region-III exhibits capacitive nature followed by Warburg impedance ( $W$ ) which corresponds to the ion diffusion kinetics at the electrode-electrolyte interface.

Figures 3(e and f) and S10(a–i), shows the self-discharge test of coin cells (boric acid coated  $\alpha\text{-MnO}_2$  electrode vs.  $\text{Li}^+/\text{Li}$ ) at various rest hours. The open circuit voltage (OCV) and resistance ( $R$ ) of the fabricated fresh coin cells are measured without applying any external load at different intervals of time period up to a week for 168 hours. Red and blue LEDs are connected with coin cells for a short period of time at each specific interval to check the intensity of light emission. The intensity of the red and blue LED is higher for fresh cells due to the low internal resistance ( $R$ ) and high OCV. The fabrication of CR2032 coin cells for powering blue and red LED with its initial OCV and  $R$  for fresh cells are shown in Supporting Information Video 1. The variation of OCV and  $R$  of the coin cells corresponding to the red and blue LEDs at various rest hours in a bar chart is shown in Figure 3(e). The self-discharge test indicates that the boric acid coated  $\alpha\text{-MnO}_2$  based coin cells are stable without any abrupt variation in internal resistance and OCV.

After self-discharge study, the same coin cells with boric acid coated  $\alpha\text{-MnO}_2$  electrodes have been used to perform continuous powering of red and blue LED lights from 312<sup>th</sup> hour as shown in Figures 4(a and b) and S11(a–i). The coin cells are taken out momentarily to record the OCV and  $R$  values at various time intervals during continuous powering of LEDs. When the coin cells are continuously connected to LEDs, intensity of the red and blue LEDs gradually fades with descending OCV and  $R$  values and intensity diminished at about ~24–32 hours, respectively. The continuous LED powering test proves that the boric acid coated  $\alpha\text{-MnO}_2$  electrodes are suitable for stable self-powering red and blue LEDs.

Once the OCV of the coin cells reached a threshold limit for the corresponding LEDs (red and blue LED), the cells are disconnected and discharged to 0.0 V at 0.1 C (Figure 4c and d). After complete discharge and charge, the corresponding OCV and  $R$  of the cells connected to the red and blue LEDs are recorded (bottom inset).

In order to check reversibility, both the cells are charged up to 3 V and subsequently connected to the respective LEDs after measuring OCV and  $R$  which indicates bright glowing with high intensity as shown in Figure 4(c and d, top inset) and Figure 4(e and f). The observed discharge capacity of coin cells with  $\text{H}_3\text{BO}_3@\alpha\text{-MnO}_2$  electrodes interestingly exhibits 1924 mAh g<sup>-1</sup>, and 2665 mAh g<sup>-1</sup> for the deeply discharged (i.e., up to 0.0 V) coin cells connected to red and blue LEDs, respectively which might be due to the depth of discharge. In most of the electrodes, SEI formation between the electrode-electrolyte acts as a barrier for ion migration in the interfacial region. In

the present study, it's predicted that the SEI layer formed at the interface layer of electrode-electrolyte might be contributing actively to the ion migration into the electrode surface without much hindrance. Understanding SEI formation and its contributions is a tricky task to be achieved. In an effort, bare and  $\text{H}_3\text{BO}_3$  coated  $\alpha\text{-MnO}_2$  electrodes after 100 cycles of charge/discharge and also the coated electrode coin cell, used for powering LED followed by a cycle of charge/discharge are taken for ex-situ post redox investigations. All the above said coin cells are decrimped and the electrodes are dried under inert atmosphere for the XRD measurements as described in electrode preparation. Figure 5(a) shows steady mode ex-situ XRD pattern of  $\alpha\text{-MnO}_2$  bare (MB-100) and coated electrodes (HM-100) after 100 cycles as well as coated  $\alpha\text{-MnO}_2$  used to power up a LED (HML) with a cycle of discharge/charge. In all the electrodes, the strong intense peaks observed at 43.298°, 50.434°, 74.133°, 89.934°, and 95.143°, corresponding to (111), (200), (220), (311), and (222) planes are attributed to Cu substrate (ICDD card No: 00-004-0836).<sup>[35,36]</sup> The weak peaks at 44.670°, 48.376°, 54.794°, and 87.297° (Figure S12), are attributed to (103), (105), (0012), and (0018) planes of carbon black (ICDD card No: 00-026-1076).<sup>[37,38]</sup> Since the cells are dismantled at charged state, none of the electrode peaks are prominent except a broad peak observed at 36.697° corresponding to (400) plane of  $\alpha\text{-MnO}_2$  electrodes. A slight hump observed in MB-100 and HML (Figure S12) at 33.614° corresponding to (111) plane might be due to the cubic phase of  $\text{Li}_2\text{O}$  (ICDD card No: 00-012-0254).<sup>[39]</sup>

The formation of  $\text{Li}_2\text{O}$  may be due to the capture of oxygen anions from the electrolyte and surface adsorbed oxygen on the electrode by mobile lithium ions. There are few new 2θ peaks appeared at 26.881°, 30.581°, 31.475°, 33.916°, 35.892°, 43.167°, 55.955°, and 58.560° corresponding to (−211), (0−21), (−221), (−012), (−212), (−104) and (−204) crystal planes of boric acid (ICDD No: 00-030-0199)<sup>[23]</sup> in both the post-redox  $\text{H}_3\text{BO}_3@\alpha\text{-MnO}_2$  electrodes which are more intense for HM-100 electrode.

There are more significant new peaks (2θ) observed at 20.258°, 21.446°, 25.971°, 28.136°, 29.595°, 39.546°, 43.671°, and 61.571° in HM-100 electrode which are attributed to (002), (011), (−202), (211), (112), (−213), (022), and (521) crystal planes of monoclinic phase of in-situ formed quasicrystal  $\text{Li}_4\text{B}_2\text{O}_5$  (ICDD card No. 00-018-0720). The appearance of  $\text{Li}_4\text{B}_2\text{O}_5$  peaks in the cycled  $\text{H}_3\text{BO}_3@\alpha\text{-MnO}_2$  electrode indicates a facile reaction between lithium cation and borate anion during continuous redox reactions. In order to confirm the quasicrystal  $\text{Li}_4\text{B}_2\text{O}_5$  formation in the SEI layer and effect of long cycling (i.e., 100 cycles), additional ex-situ experiments such as cross section HRSEM, and FTIR analyses have been performed.

A high-resolution cross-section HRSEM has been performed on all the  $\alpha\text{-MnO}_2$  electrodes after redox reaction to understand the inner layers of SEI formation on the surface of electrodes. Figure 5(b–d) shows HRSEM cross-section images taken at 90° angle for the post-redox  $\alpha\text{-MnO}_2$  electrodes. The cross-section HRSEM images of MB-100 and HML electrodes (Figure 5b and c) indicate a bottom layer of working electrode and an uneven top SEI layer which might be due to intermetallic lithium compounds especially  $\text{Li}_2\text{O}$  as confirmed by ex-

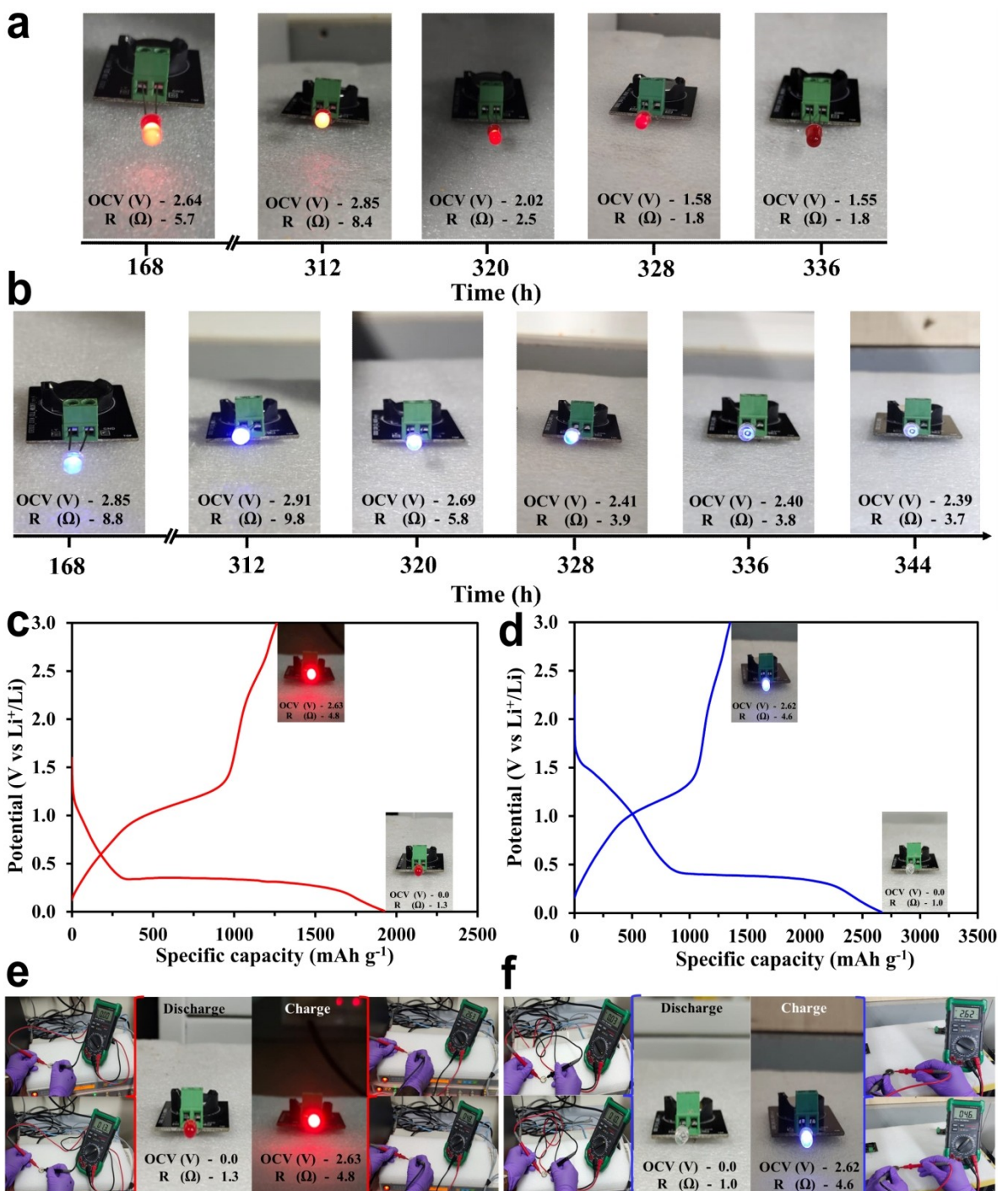


**Figure 4.** Digital images of CR2032 coin cells with  $\text{H}_3\text{BO}_3@\alpha\text{-MnO}_2$  electrode versus  $\text{Li}^+/\text{Li}$  showing continuous powering of a) red and b) blue light-emitting diodes (LEDs) with corresponding OCV and R values. Single discharge/charge test of  $\text{H}_3\text{BO}_3@\alpha\text{-MnO}_2$  electrode vs.  $\text{Li}^+/\text{Li}$  and subsequently the CR2032-coin cells connected with c) red, and d) blue LEDs after discharge/charge. Digital images of coin cells connected with e) red and f) blue LEDs after discharge and charge.

situ XRD. In the case of HM-100 electrode, the cross-section image (Figure 5d) clearly illustrates a thick SEI formation on the surface of  $\text{H}_3\text{BO}_3@\alpha\text{-MnO}_2$  which might be due to quasicrystal  $\text{Li}_4\text{B}_2\text{O}_5$  active layer as discussed in XRD and FTIR investigations. In order to probe the nature of the SEI layer, an EDX elemental mapping analysis throughout the cross-section of the electro-

des has been performed and the results are shown in Figure 5(e-g). The elemental mapping in the cross-section region of MB-100 (Figure 5e) clearly indicates homogeneous distributions of prime elements such as manganese and oxygen which confirms the presence of bare  $\alpha\text{-MnO}_2$  layer in comply with the XRD results. As shown in Figure 5(h), the EDX

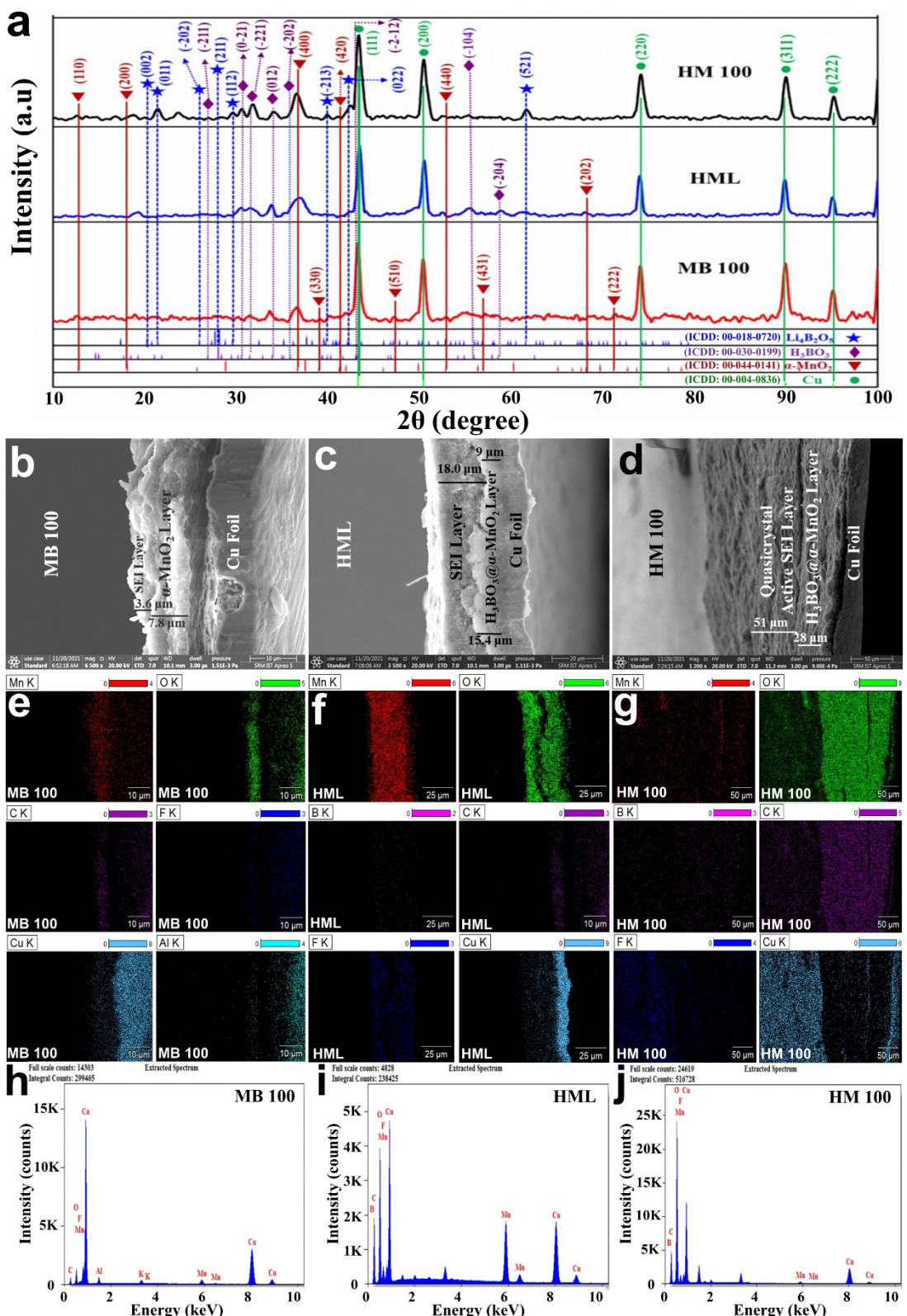


**Figure 5.** a) Steady mode ex-situ XRD plot of bare  $\alpha$ -MnO<sub>2</sub> (MB-100),  $\text{H}_3\text{BO}_3@{\alpha-\text{MnO}_2}$  (HM-100) working electrodes after 100 cycles, and  $\text{H}_3\text{BO}_3@{\alpha-\text{MnO}_2}$  electrode in coin cell used to power LED followed by a single discharge-charge (HML) vs. Li<sup>+</sup>/Li. HRSEM cross-section morphology of dismantled b) MB-100, c) HML, and d) HM-100. e–g) Cross-section elemental mapping demonstrates the distribution of elements such as Mn, O, B, C, F, Cu, and Al in post-cycled electrodes. h–j) Energy Dispersive X-ray (EDX) spectra of the  $\alpha$ -MnO<sub>2</sub> based post-redox electrodes.

spectrum of MB-100 is very well reflecting the existence and distribution of the elements Mn, O, C, F and Cu as that of elemental mapping. Figure 5(f) shows elemental mapping of HML in the cross-section region indicates distribution of elements such as Mn, O, B, C, F and Cu. Rich Mn and O contents in the sample region reveals presence of  $\alpha\text{-MnO}_2$  layer in  $\text{H}_3\text{BO}_3@\alpha\text{-MnO}_2$ . It's interesting to note that the boron element spread from the  $\alpha\text{-MnO}_2$  layer to the top SEI layer which reveals the formation of amorphous  $\text{Li}_4\text{B}_2\text{O}_5$  at the electrode-electrolyte interface might have initiated once the redox process started that gets developed into quasicrystal upon continuous redox cycles as found in ex-situ XRD of HM-100. The EDX spectrum (Figure 5i) clearly projects the rich content of prime sample elements such as Mn, O, and B.

Figure 5(g) shows elemental mapping of HM-100 which indicates the presence of B, Mn, and O elements distributed evenly across the cross-section due to the slanted view. It's worthy to note that the even distribution of boron and oxygen in the sample region to the top SEI layer might be due to the Li-B-O boron compound formation as discussed in post-redox XRD analysis. Figure 5(j) depicts EDX spectrum of the HM-100 electrode which confirms the rich content of Mn, O, B active elements along with minor peaks of C and F. In all the above elemental mapping and EDX spectra, the presence of C, F and Cu elements might be sourced from carbon black (conducting agent) as well as PVDF (binder) that are used to prepare the electrode slurry and the copper current collector, respectively. In addition, the elemental mapping images indicate the presence of 'Al' which might be due to the aluminum HRSEM stub. The elemental mapping of post-redox  $\text{H}_3\text{BO}_3@\alpha\text{-MnO}_2$  electrodes clearly reveals the presence of boron compound in the sample as well as in SEI layer which reveals the formation of lithium inter-metallic compound with boron as discussed in ex-situ XRD investigations.

The broad ex-situ FTIR spectrum (Figure 6a) indicates absorption peaks of  $\text{MnO}_2$ ,  $\text{H}_3\text{BO}_3$ ,  $\text{Li}_2\text{O}$ , PVDF binder, carbon black, and solvent traces as briefed in Table S3, supporting information. In order to analyse the specific vibrational bands, the FTIR spectrum is magnified into three regions as shown in Figure 6(b-d). The FTIR spectrum of region-I indicates strong and broad absorption peak at 463–470  $\text{cm}^{-1}$  corresponding to stretching vibration of Mn–O–Mn bond (Figure 6b) in all the three post-redox  $\alpha\text{-MnO}_2$  based electrodes.<sup>[40,41]</sup> Furthermore, strong absorption peaks observed at 482–488  $\text{cm}^{-1}$  are attributed to stretching vibrational mode of Mn–O bonds.<sup>[42]</sup> These Mn–O stretching vibrations gets slightly shifted in all the three samples due to the electrochemical alterations of  $\alpha\text{-MnO}_2$  upon redox reactions. The broad absorption peak observed at ~475–480  $\text{cm}^{-1}$  in all the samples is attributed to Li–O stretching vibration which indicates the formation of SEI layer.<sup>[43]</sup>

In region-II, broad absorption peak observed at 709–720  $\text{cm}^{-1}$  is attributed to the stretching vibrations of Mn–O–Mn bond in all the post-redox electrodes (Figure 6c).<sup>[44]</sup> A strong absorption peak observed at ~1060–1070  $\text{cm}^{-1}$  is assigned to the stretching mode of Mn–O bond. Strong absorption peaks observed at ~1011–1020 and ~1125–1145  $\text{cm}^{-1}$  are attributed

to the Li–O stretching modes of  $\text{Li}_2\text{O}$  in all the cycled samples.<sup>[45]</sup>

In region-III (Figure 6d), the absorption peaks observed in the region at 1245–1253, and 1355  $\text{cm}^{-1}$  are attributed to symmetric stretching vibrations of B–O bond in  $\text{BO}_3$  units for HM-100 electrodes. The shifting in peak positions of B–O and Li–O vibration bands in redox cycled HM-100 electrodes indicate that there might be a facile compound formation between Li–O–B which is also evidenced from ex-situ investigations by the presence of quasicrystal  $\text{Li}_4\text{B}_2\text{O}_5$  (XRD) and boron presence in SEI layer (SEM).

Based on the cumulative experimental evidences and considering the nature of facile bond making possibilities of boron with oxygen and  $\text{Li}^+$  ion, its confirmed that the surface boron might have involved in a network bond formation with 'O' and 'Li' as  $\text{Li}_4\text{B}_2\text{O}_5$  in the post-redox  $\text{H}_3\text{BO}_3@\alpha\text{-MnO}_2$  electrodes as illustrated in Figure 6(e).

As evidenced from ex-situ investigations, the  $\text{H}_3\text{BO}_3@\alpha\text{-MnO}_2$  electrode gets developed an active  $\text{Li}_4\text{B}_2\text{O}_5$  based SEI layer at the electrode-electrolyte interface upon prolonged redox cycles (i.e., 100 cycles) which effectively support for the  $\text{Li}^+$  ion migration and effectively alleviates the pile-up of inactive  $\text{Li}_2\text{O}$  and  $\text{Li}_2\text{CO}_3$  layers at the interface. The ex-situ investigations confirmed the active SEI layer formation which could be the reason behind high coulombic efficiency observed in  $\text{H}_3\text{BO}_3@\alpha\text{-MnO}_2$  electrode after 60 cycles.  $\text{H}_3\text{BO}_3@\alpha\text{-MnO}_2$  electrode proved an excellent lithium-ion storage performance, and with that motivation, an effort has been made to further investigate the boric acid coated electrode performance in symmetry FTSC device. Figure 7(a) shows electrochemical studies of symmetric FTSC device (two electrode system) with  $\text{H}_3\text{BO}_3@\alpha\text{-MnO}_2$  electrode in the potential range of 0.0 to 1.2 V at various scan rates. The CV curves are not exactly rectangular in shape but attributed to the redox processes corresponding to  $\text{H}_3\text{BO}_3@\alpha\text{MnO}_2$  indicates pseudocapacitive behavior. The CV curve exhibits a pair of broad oxidation peaks in the region of 0.29–0.59 V, 0.8–1.1 V and reduction peaks at 0.9–0.51 V, 0.5–0.1 V with the increment in sweep rates from 10 to 500  $\text{mV s}^{-1}$ .

There is no abrupt peak difference in the first redox couple which indicates an excellent reversibility between electrodes. The second redox couple in the region of 0.51–1.1 V shows a wider peak splitting of about 0.31 V, which is ascribed to the quasi-reversible nature of the electrode at high scan rate. This behavior is related to  $(\text{OH})^-$  ion capturing by boric acid which may not affect the overall reversibility of the electrode. These redox peak shifts with respect to the increase in sweep rates might be due to effective mass (ionic species) and electron transfer that leads to polarization in the electrode materials. The oxidation-reduction peaks are shifting together towards lower potential with the increase in scan rate which is attributed to the electrochemical alteration of the electrode.

The appearance of two redox couple in the CV plot reveals that there might be existence of two phases in the  $\text{H}_3\text{BO}_3@\alpha\text{-MnO}_2$  compound. The first redox couple observed in the range of 0.1 to 0.59 V indicates the redox reaction due to the transition of Mn in  $\text{MnO}_2$  from  $\text{Mn}^{4+}$  to  $\text{Mn}^{3+}$  reduction and

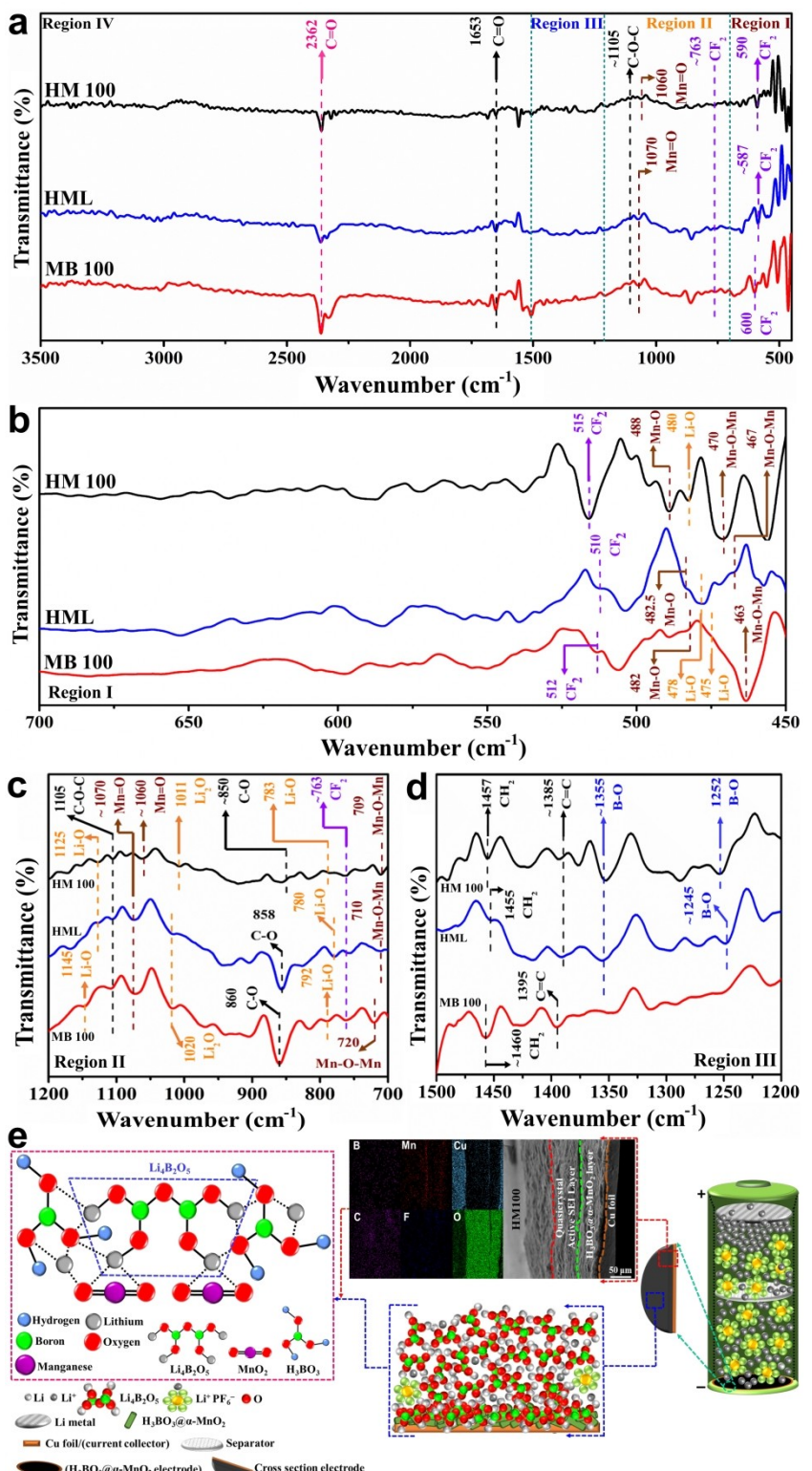


**Figure 6.** a) Ex-situ FTIR spectra of decrimped bare and H<sub>3</sub>BO<sub>3</sub> coated α-MnO<sub>2</sub> electrodes (MB-100, HML, HM-100). Magnified FTIR spectrum in b) Region-I (450 to 700 cm<sup>-1</sup>), c) Region-II (700 to 1200 cm<sup>-1</sup>), and d) Region-III (1200 to 1500 cm<sup>-1</sup>). e) Scheme for cross-section of post-cycled H<sub>3</sub>BO<sub>3</sub>@α-MnO<sub>2</sub> electrode showing components of active SEI layer along with molecular structure of the quasicrystal Li<sub>4</sub>B<sub>2</sub>O<sub>5</sub> formation in the SEI layer and its interactions.

Mn<sup>3+</sup> to Mn<sup>4+</sup> oxidation in order to accommodate the cation species (H<sup>+</sup> ion) from the aqueous KOH and de-intercalate, respectively. Each of this univalent H<sup>+</sup> ion intercalation in to

α-MnO<sub>2</sub> might store one electron. This redox reaction is completely reversible as evidenced from the CV curves. The appearance of second redox couple indicates that there might

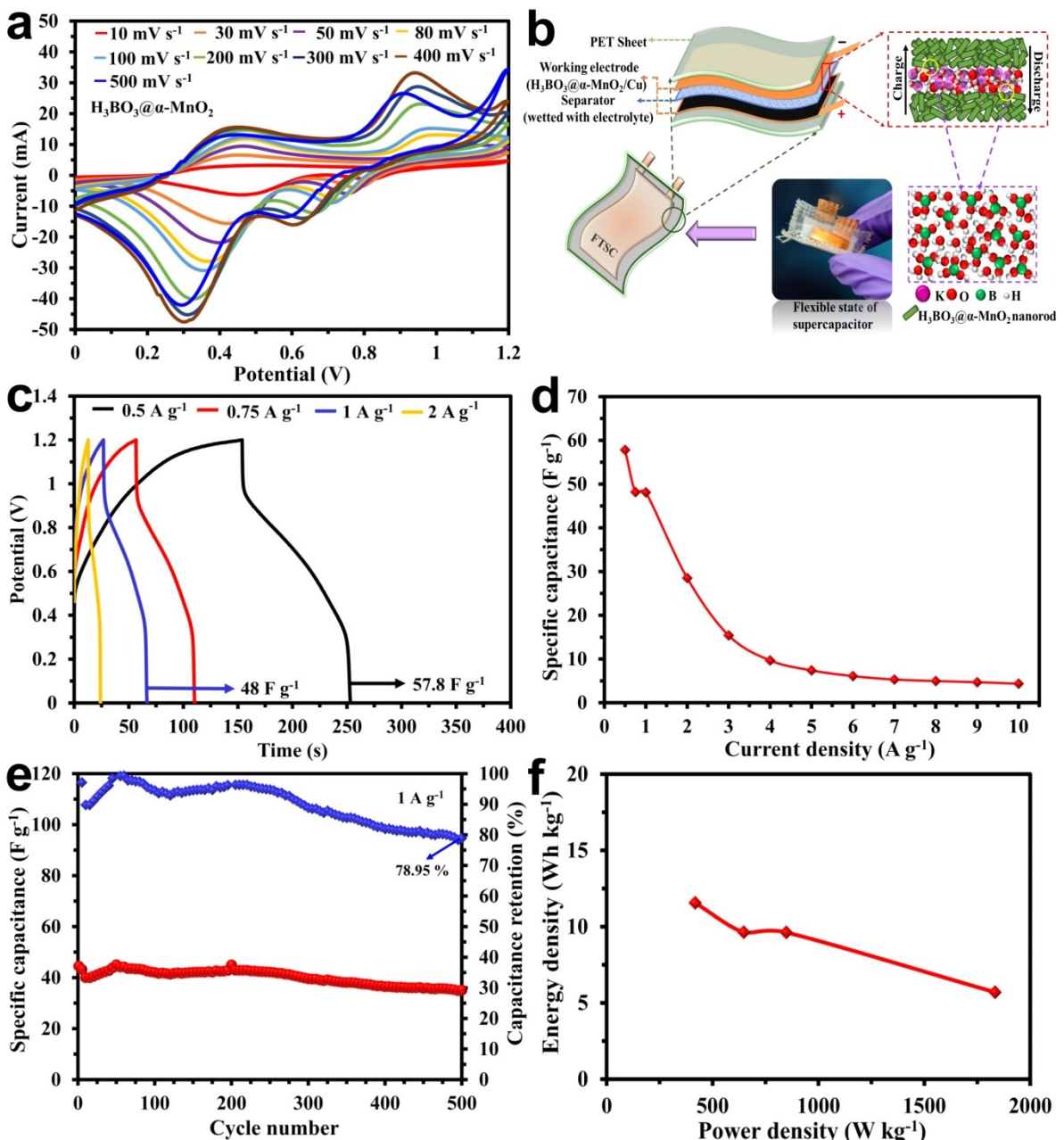


**Figure 7.** a) CV performance of the FTSC device with  $\text{H}_3\text{BO}_3@\alpha\text{-MnO}_2$  at various sweep rates (10–500  $\text{mV s}^{-1}$ ). b) Digital image of FTSC device, a scheme of FTSC layered architecture, and microscopic molecular structure view of electrode-electrolyte in FTSC during charge/discharge. c) Galvanostatic charge/discharge profile of FTSC device at different current densities (0.5–2)  $\text{A g}^{-1}$ . d) Specific capacitance variation of the FTSC device at various current densities. e) Cycling performance of the FTSC device at 1  $\text{A g}^{-1}$  with simultaneous variation in the capacitance retention. f) Ragone plot of FTSC device.

be another redox kinetics which may be due to the boric acid reaction kinetics with  $\text{H}_2\text{O}$  and KOH at relatively high potential (i.e., 0.51–1.1 V). The two possibilities of  $\text{B(OH)}_3$  reaction with  $\text{H}_2\text{O}$  and KOH are as follows,



The KOH in aqueous solution might be in dissociated form as  $\text{K}^+$  and  $(\text{OH})^-$  and the anion react with boric acid as follows,



In aqueous KOH solution, boric acid acts like a Lewis acid which could be ionized through the boron-oxygen bond by quickly breaking and forming the bond spontaneously. Boric acid facilitates capture of  $(\text{OH})^-$  from the electrolyte and allows the  $\text{H}^+$  ion to migrate through boric acid layer to reach  $\text{MnO}_2$ . This reaction proceeds by reversible accommodation of an  $(\text{OH})^-$  ion through facile boron-oxygen bond breaking and formation which might be the reason for second quasi

reversible redox couple. Figure 7(b) depicts a digital image of bent FTSC and schematic of FTSC device with microscopic molecular structure view of electrode-electrolyte in FTSC during charge/discharge which indicates ease of reaction possibilities of  $\text{B}(\text{OH})_3$  with  $\text{H}_2\text{O}/(\text{OH})^-$  as in Equations (2) and (3).

The broad redox peaks observed in the CV curves are indicating the pseudo-capacitive properties of the well-assembled FTSC device with symmetry  $\text{H}_3\text{BO}_3@\alpha-\text{MnO}_2$  electrodes. It's interesting to note that the redox peak current increases by increasing the sweep rate which is due to the current proportionality with the square root of scan rate. The increasing trend of redox peak current with increase of scan rate indicates higher diffusivity rate as per Randles-Sevcik equation. The CV curves exhibit a large area under the redox peak, which is proportional to the quantity of charge storage of the electrode material. The significant results such as redox repeatability, relatively good redox peak retention and increasing trend of redox peak current at higher scan rates strongly suggests the electrochemical stability and excellent reversibility of  $\text{H}_3\text{BO}_3@\alpha-\text{MnO}_2$ .

Galvanostatic charge/discharge (GCD) plot (Figure 7c) at different current densities depicts a typical quasi triangular curve with longest discharging time which suggests occurrence of Faradic pseudocapacitance reaction and excellent electrochemical properties of the fabricated electrodes. The specific capacitance of the FTSC device is calculated from the time versus potential GCD plots by using Equation (4).<sup>[46,47]</sup>

$$C_s = - \frac{I}{m \frac{dV}{dt}} \quad (4)$$

where 'I' is the constant applied current (mA), 'm' is the sum of the total masses of the two electrodes (g),  $dV/dt$  ( $\text{Vs}^{-1}$ ) is obtained from slope of the discharge curve by fitting a straight line. The range of potential (V) is taken by excluding the IR drop. The FTSC device exhibits specific capacitance ( $C_s$ ) of 57.8 and 48  $\text{F g}^{-1}$  with respect to current densities of 0.5 and 1  $\text{A g}^{-1}$ , respectively. The time versus potential GCD curve (Figure S13) at different current densities (3 to 10  $\text{A g}^{-1}$ ) indicates gradual decrease in specific capacitance by increasing current density which is due to the increase in IR drop. The specific capacitance is decreasing gradually with the increase of current density (Figure 7d) which might be due to the fast redox kinetics in the system. The specific capacity of the FTSCs is calculated by using Equation (5).<sup>[48]</sup>

$$Q = C_s \times \Delta V \quad (5)$$

where Q is the specific capacity ( $\text{Cg}^{-1}$ ) and  $\Delta V$  is the potential window (V). The calculated specific capacity of the device is 70, 58, 58, and 34  $\text{Cg}^{-1}$  at 0.5, 0.75, 1 and 2  $\text{A g}^{-1}$ , respectively. Figure 7(e) shows the cyclic performance of the FTSC device at a constant current density of 1  $\text{A g}^{-1}$  for 500 cycles. It's interesting to note that the initial specific capacitance of 44.5  $\text{F g}^{-1}$  is almost stable up to 270<sup>th</sup> cycle with capacitance retention (CR) of 94.5% which then gradually decreases to 35  $\text{F g}^{-1}$  at 500<sup>th</sup> cycle with 78.9% CR. The obtained capacitance

of  $\text{H}_3\text{BO}_3@\alpha-\text{MnO}_2$  is comparable with other  $\text{MnO}_2$  based electrodes studied for supercapacitor applications as listed in the Table S4. However, the reason for relatively low value of specific capacitance might be due to the inclusion of inseparable weight of  $\text{H}_3\text{BO}_3$  with the active  $\alpha-\text{MnO}_2$ . It's expected that there might be feasible  $\text{H}^+$  ion migration pathways through boric acid due to the  $\text{B}(\text{OH})_4^-$  formation. The electro-negative oxygen of  $\text{MnO}_2$  interacts with  $\text{H}^+$  ionic species and manganese gets reduced from  $\text{Mn}^{4+}$  to  $\text{Mn}^{3+}$  in order to accommodate the ionic species which leads to increases in capacitance. The boric acid not only prevents deterioration in  $\text{MnO}_2$  electrodes that also plays an important role as  $(\text{OH})^-$  ion capturing as discussed in the CV analysis. The synergistic effect produced by boric acid and reversible 'Mn' transitions drives the device with excellent electrochemical stability for numerous redox cycling as shown in the Figure 7(e). The energy density and power density values of FTSC device with  $\text{H}_3\text{BO}_3@\alpha-\text{MnO}_2$  symmetry electrodes at different current densities (0.5 to 2  $\text{A g}^{-1}$ ) are calculated from the GCD plot and the results are illustrated in a Ragone plot as shown in Figure 7(f).

The energy density ( $E$  in  $\text{Wh kg}^{-1}$ ) of the device is calculated by using Equation (6).<sup>[49]</sup>

$$E = \frac{1000 \times C_s \times (\Delta V)^2}{2 \times 3600} \quad (6)$$

where  $\Delta V$  is the potential window in (V)

The power density ( $P$  in  $\text{W kg}^{-1}$ ) of the device is calculated by using Equation (7)

$$P = \frac{E}{t_d} \times 3600 \quad (7)$$

where  $t_d$  is the discharge time. As observed from the Ragone plot, the power density is decreasing when the energy density increases and vice-versa which reveals a typical supercapacitor behavior. The optimum energy density and power density of the FTSC device are found to be 11.56  $\text{Wh kg}^{-1}$  and 1833.4  $\text{kW kg}^{-1}$ , respectively.

Figure 8(a) shows CV plot for the FTSC device (used for 500 cycles) at a bending angle of 30° at a scan rate of 100  $\text{mVs}^{-1}$ . The CV curves of the flexible device after bending are in concurrence with the CV results obtained before bending. The appearance of broad redox peaks corresponding to the  $\text{H}_3\text{BO}_3@\alpha-\text{MnO}_2$  electrode indicates pseudocapacitive nature. The CV peaks obtained for both bending angles are exactly overlapping without any characteristic changes and also resembling with the results obtained before bending, which reveals that the electrochemical properties of FTSC device are not affected by the bending angles.

The CV plot is also evidenced that the electrodes in FTSC device are highly stable with bending angles. The same FTSC device is bent at 30° to carry out CV measurements at various scan rates as shown in Figure 8(b). It is interesting to note that though the device is used for long cycling and bending tests, still the CV curves exhibit similar redox response as that of

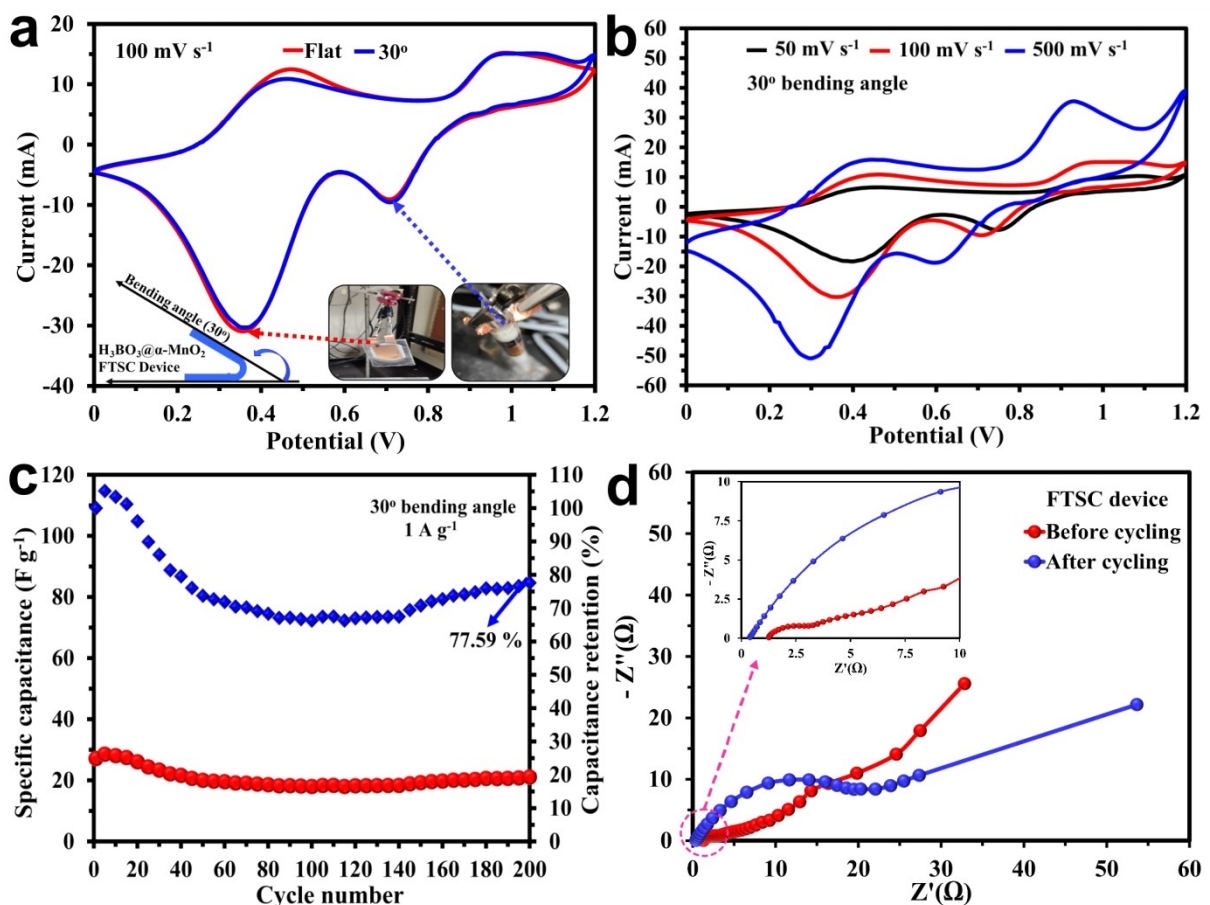


**Figure 8.** a) A comparison CV plot (after 500 cycles) of FTSC device in flat and 30° bending angles at 100 mV s<sup>-1</sup>. b) CV plot of 30° bent device at various sweep rate. c) Cycling stability of 30° bent FTSC device at the current density of 1 A g<sup>-1</sup> along with capacitance retention. d) Nyquist plot of FTSC device before and after cycling (Inset: Zoomed at high frequency region).

before bending device without any changes in the characteristics of the peaks.

In addition, the same device has been used to measure the cyclic stability under a 30° bending angle state for 200 cycles at a constant current density of 1 A g<sup>-1</sup> as shown in Figure 8(c). The initial specific capacitance of the device is found to be 27.1 F g<sup>-1</sup> with capacitance retention of 100%. Despite slight initial capacitance fluctuations, the specific capacitance is found to be very stable up to 200<sup>th</sup> cycle with the capacitance of 21 F g<sup>-1</sup> and capacitance retention of 77.6%. This predominant endurance of the FTSC device at different bending angles reveals excellent stability and reversibility of the H<sub>3</sub>BO<sub>3</sub>@α-MnO<sub>2</sub> electrode. The Nyquist plot (Figure 8d) of the FTSC device after several cycles indicates a development of internal solution resistance ( $R_s$ ) and charge transfer resistance ( $R_{ct}$ ) that might be due to the decrease in concentration of aqueous KOH electrolyte by evaporation which gets reflected as drop in specific capacitance. Briefly, the careful evaluation of constructed FTSC device with flexible H<sub>3</sub>BO<sub>3</sub>@α-MnO<sub>2</sub> electrodes exhibits an excellent electrochemical cycling stability, rate capability and endurance with different bending angles.

## Conclusion

In this article, the benefits of H<sub>3</sub>BO<sub>3</sub> coating over α-MnO<sub>2</sub> nanorods related to the electrochemical performance have been discussed in detail. The H<sub>3</sub>BO<sub>3</sub> coated α-MnO<sub>2</sub> electrode reveal polycrystalline nature with grain size of 21.1 nm as confirmed by XRD analysis. HRSEM morphological analysis confirms nanorod formation with a range of length ~350–50 nm and diameter ~30–35 nm for the boric acid coated α-MnO<sub>2</sub>. The HRTEM morphology investigations of H<sub>3</sub>BO<sub>3</sub>@α-MnO<sub>2</sub> reveal elegant α-MnO<sub>2</sub> nanorod formation with a fine boric acid coating of 5–6 nm thickness. The SAED pattern of H<sub>3</sub>BO<sub>3</sub>@α-MnO<sub>2</sub> confirms the formation of two different polycrystalline structures corresponding to boric acid and α-MnO<sub>2</sub> nanorod while the XPS investigations confirm the presence of Mn, O and B elements in H<sub>3</sub>BO<sub>3</sub>@α-MnO<sub>2</sub>. The deconvolution of Mn 2p<sub>3/2</sub> and Mn 2p<sub>1/2</sub> signals observed in XPS of α-MnO<sub>2</sub> electrodes prove the existence of two prominent oxidation states of Mn<sup>+4</sup> and Mn<sup>+3</sup>.

The cyclic voltammetry results of α-MnO<sub>2</sub> bare and H<sub>3</sub>BO<sub>3</sub>@α-MnO<sub>2</sub> nanorods indicate well defined redox peaks with good reversibility. The charge/discharge results show that the initial discharge capacity observed for α-MnO<sub>2</sub> bare and

$\text{H}_3\text{BO}_3@\alpha-\text{MnO}_2$  nanorod is 953.6 and 1288  $\text{mAh g}^{-1}$ , respectively. The cycling study of  $\text{H}_3\text{BO}_3@\alpha-\text{MnO}_2$  electrode at 1 C rate shows an excellent electrochemical stability even after 60<sup>th</sup> cycle with discharge capacity of 76  $\text{mAh g}^{-1}$  and 100% coulombic efficiency until 100<sup>th</sup> cycle which is relatively better than that of bare  $\alpha-\text{MnO}_2$ . The  $\text{H}_3\text{BO}_3@\alpha-\text{MnO}_2$  electrode exhibits high lithium-ion diffusion kinetics ( $D_{\text{Li}^+} \sim 10^{-10} \text{ cm}^2 \text{s}^{-1}$ ) that leads to the significant enhancement in the electrochemical performance. The enhanced cycling stability might be due to the self-assembled quasicrystal  $\text{Li}_4\text{B}_2\text{O}_5$  active interfacial layer formation at the electrode-electrolyte interface upon continuous cycling as evidenced from the ex-situ analyses. The endurance against high C-rate observed in both  $\alpha-\text{MnO}_2$  electrodes might be due to the high tensile strength of nanorod architecture which provides high stability against continuous  $\text{Li}^+/\text{Li}$  redox reactions even at high current rate. The boric acid coating protects the  $\alpha-\text{MnO}_2$  nanorods from electrode deterioration and rupture on the electrode surface. The self-discharge test of lithium-ion coin cell with  $\text{H}_3\text{BO}_3@\alpha-\text{MnO}_2$  shows a highly stable OCV negligible internal cell resistance variation over 168 hours. Subsequently the coin cells are used to power-up red and blue LEDs which indicate a stable continuous self-sustainable powering for about 32 hours. An in-depth ex-situ XRD, HRSEM and FTIR investigations on post-redox cycled  $\text{H}_3\text{BO}_3@\alpha-\text{MnO}_2$  electrodes exemplify the formation of quasicrystal  $\text{Li}_4\text{B}_2\text{O}_5$  as an active SEI layer on the surface of electrode which leads to the effective  $\text{Li}^+$  ion migration at the electrode-electrolyte interface.

The outperformed  $\text{H}_3\text{BO}_3@\alpha-\text{MnO}_2$  electrode material has also been used to fabricate a flexible and transparent supercapacitor device. The fabricated flexible device demonstrated a long-time cyclic stability up to 500 cycles at 1  $\text{Ag}^{-1}$  with specific capacitance of 35  $\text{F g}^{-1}$  and capacity retention of 78.9% which is only 21% fading of initial capacitance. The FTSC device with symmetry  $\text{H}_3\text{BO}_3@\alpha-\text{MnO}_2$  electrodes exhibits excellent specific capacitance of 57.81, 48.1  $\text{F g}^{-1}$  at different current densities of 0.5, 1  $\text{Ag}^{-1}$ , respectively. The optimal energy and power density of the device are 11.56  $\text{Wh kg}^{-1}$  and 1833  $\text{W kg}^{-1}$ , respectively. The electrochemical evaluation of flexibility framework at 30° bending angle of the FTSC device reveals that the electrochemical property of the device is not interrupted even at large acute angles which proves the excellent efficiency of flexible device. In nutshell, the  $\text{H}_3\text{BO}_3@\alpha-\text{MnO}_2$  nanorod electrodes are most suitable for energy storage device applications specifically in LIBs and next generation flexible supercapacitors. The interesting reaction kinetics of Li-O-B followed by an active quasicrystal  $\text{Li}_4\text{B}_2\text{O}_5$  SEI layer formation leads to a motivation for future studies towards construction of a complete solid-state lithium-boron battery.

## Acknowledgements

This work was financially supported by the Department of Science and Technology-Science and Engineering Research Board (DST-SERB), New Delhi, India (File No: ECR/2017/000095/ES). The authors would like to acknowledge Mr. Vadivel, Senior Scientific

Officer (HRTEM), and Mr. Vaitheswaran, Junior Scientific Officer (HRSEM) from SRM Central Instrumentation Facility (SCIF), from SRMIST. Also, authors would like to thank Ex-situ XRD and XPS from Department of Physics, and Nanotechnology Research Centre (NRC) from SRMIST. The authors gratefully thank Mr. Dharmaraj (FTIR), from Department of Chemistry, SRMIST, Kattankulathur-603 203, Tamil Nadu, Chennai, India.

## Conflict of Interest

The authors declare no conflict of interest

## Data Availability Statement

The data that support the findings of this study are available from the corresponding author upon reasonable request.

**Keywords:**  $\alpha-\text{MnO}_2$  • active quasicrystal interfacial layer • flexible supercapacitor • lithium-ion cells • nanorods • powering LEDs

- [1] Y. Meng, Y. Liu, J. He, X. Sun, A. Palmieri, Y. Gu, X. Zheng, Y. Dang, X. Huang, W. Mustain, S. L. Suib, *ACS Appl. Energ. Mater.* **2021**, *4*, 5424–5433.
- [2] Y. Wang, B. Liu, Q. Li, S. Cartmell, S. Ferrara, Z. D. Deng, J. Xiao, *J. Power Sources* **2015**, *286*, 330–345.
- [3] S. J. Kim, Y. J. Yun, K. W. Kim, C. Chae, S. Jeong, Y. Kang, S. Y. Choi, S. S. Lee, S. Choi, *ChemSusChem* **2015**, *8*, 1484–1491.
- [4] S. C. Weng, S. Brahma, P. C. Huang, Y. C. Huang, Y. H. Lee, C. C. Chang, J. L. Huang, *Appl. Surf. Sci.* **2020**, *505*, 144629.
- [5] J. Chen, Y. Wang, X. He, S. Xu, M. Fang, X. Zhao, Y. Shang, *Electrochim. Acta* **2014**, *142*, 152–156.
- [6] Y. Chu, L. Guo, B. Xi, Z. Feng, F. Wu, Y. Lin, J. Liu, D. Sun, J. Feng, Y. Qian, S. Xiong, *Adv. Mater.* **2018**, *30*, 1707572.
- [7] K. Cao, Y. Jia, S. Wang, K. Huang, H. Liu, *J. Alloys Compd.* **2021**, *854*, 157179.
- [8] Y. Gong, L. Sun, H. Si, Y. Zhang, Y. Shi, L. Wu, J. Gu, Y. Zhang, *Appl. Surf. Sci.* **2020**, *504*, 144479.
- [9] Z. Zhou, D. Chaoying, P. Wenchao, L. Yang, Z. Fengbao, F. Xiaobin, *J. Mater. Sci. Technol.* **2021**, *80*, 13–19.
- [10] Z. Tong, Y. Yuan, S. Yin, B. Wang, M. Zhu, S. Guo, *Sustain. Mater. Technol.* **2021**, *29*, e00312.
- [11] J. Yoon, W. Choi, T. Kim, H. Kim, Y. Seok Choi, J. Man Kim, W. S. Yoon, *J. Energy Chem.* **2020**, *53*, 276–284.
- [12] Y. Zhang, H. Liu, Z. Zhu, K. W. Wong, R. Mi, J. Mei, W. M. Lau, *Electrochim. Acta* **2013**, *108*, 465.
- [13] M. G. Kim, J. Cho, *Adv. Funct. Mater.* **2009**, *19*, 1497–1514.
- [14] Z. Liu, W. Zhou, J. He, H. Chen, R. Zhang, Q. Wang, Y. Wang, Y. Yan, Y. Chen, *J. Alloys Compd.* **2021**, *869*, 159279.
- [15] J. Song, Y. Li, R. Tong, Y. Yan, Q. Tian, J. Chen, L. Yang, *J. Phys. Chem. Solids* **2022**, *160*, 110317.
- [16] M. H. Alfarouqi, J. Gim, S. Kim, J. Song, J. Jo, S. Kim, V. Mathew, J. Kim, *J. Power Sources* **2015**, *288*, 320–327.
- [17] Z. Li, J. Wang, Z. Wang, Y. Tang, C. S. Lee, S. Yang, *RSC Adv.* **2014**, *4*, 54416–54421.
- [18] A. J. C. Mary, C. I. Sathish, A. Vinu, A. C. Bose, *Energy Fuels* **2020**, *34*, 10131–10141.
- [19] S. Dong, G. Xie, A. Huo, R. Yin, *Ionics* **2022**, *28*, 2197.
- [20] Z. Wu, W. Ren, L. Wen, L. Gao, J. Zhao, Z. Chen, G. Zhou, F. Li, H. Cheng, *2010*, *4*, 3187–3194.
- [21] T. Cetinkaya, M. Tokur, S. Ozcan, M. Uysal, H. Akbulut, *Int. J. Hydrogen Energy* **2016**, *41*, 6945–6953.
- [22] R. Bi, G. Liu, C. Zeng, X. Wang, L. Zhang, S. Z. Qiao, *Small* **2019**, *15*, 1804958.

- [23] S. İpeksever, M. Gönen, *J. Supercrit. Fluids* **2020**, *166*, 104998.
- [24] K. Ahmad, A. Mohammad, S. M. Mobin, *Electrochim. Acta* **2017**, *252*, 549–557.
- [25] G. Xie, X. Liu, Q. Li, H. Lin, Y. Li, M. Nie, L. Qin, *J. Mater. Sci.* **2017**, *52*, 10915.
- [26] M. Du, Y. Bu, Y. Zhou, Y. Zhao, S. Wang, H. Xu, *RSC Adv.* **2017**, *7*, 12711–12718.
- [27] M. Han, J. Huang, S. Liang, L. Shan, X. Xie, Z. Yi, Y. Wang, S. Guo, J. Zhou, *iScience* **2020**, *23*, 100797.
- [28] T. Shen, *J. Mater. Sci.* **2019**, *54*, 8852–8859.
- [29] Q. Wang, H. Pang, Y. Dong, Y. Chi, F. Fu, *Microchim. Acta* **2018**, *185*, 1.
- [30] H. Kim, N. Venugopal, J. Yoon, W. S. Yoon, *J. Alloys Compd.* **2019**, *778*, 37–46.
- [31] A. L. M. Reddy, M. M. Shajumon, S. R. Gowda, P. M. Ajayan, *Nano Lett.* **2009**, *9*, 1002–1006.
- [32] J. Huang, Z. Wang, M. Hou, X. Dong, Y. Liu, Y. Wang, Y. Xia, *Nat. Commun.* **2018**, *9*, 1.
- [33] D. Sun, J. Chen, J. Yang, X. Yan, *CrystEngComm* **2014**, *16*, 10476–10484.
- [34] Y. Qin, J. Lu, P. Du, Z. Chen, Y. Ren, T. Wu, J. T. Miller, J. Wen, D. J. Miller, Z. Zhang, K. Amine, *Energy Environ. Sci.* **2013**, *6*, 519–531.
- [35] P. Xu, K. Ye, M. Du, J. Liu, K. Cheng, J. Yin, G. Wang, D. Cao, *RSC Adv.* **2015**, *5*, 36656–36664.
- [36] L. Xiong, S. Huang, X. Yang, M. Qiu, Z. Chen, Y. Yu, *Electrochim. Acta* **2011**, *56*, 2735–2739.
- [37] N. Raeisi-Kheirabadi, A. Nezamzadeh-Ejhieh, H. Aghaei, *Microchem. J.* **2021**, *162*, 105869.
- [38] N. Raeisi-Kheirabadi, A. Nezamzadeh-Ejhieh, H. Aghaei, *Surfaces Interfaces* **2021**, *27*, 101484.
- [39] J. Zhao, J. Sun, A. Pei, G. Zhou, K. Yan, Y. Liu, D. Lin, Y. Cui, *Energy Storage Mater.* **2018**, *10*, 275–281.
- [40] L. Jiang, S. Xiao, J. Chen, *Colloids Surf. A* **2015**, *479*, 1.
- [41] R. Jokar, S. M. Alavi, M. Rezaei, E. Akbari, *Int. J. Hydrogen Energy* **2021**, *46*, 32503–32513.
- [42] N. Kumar, P. Dineshkumar, R. Rameshbabu, A. Sen, *Mater. Lett.* **2015**, *158*, 309–312.
- [43] I. Kashif, A. A. Soliman, E. M. Sakr, A. Ratep, *Spectrochim. Acta Part A* **2013**, *113*, 15–21.
- [44] Y. Li, J. Wang, Y. Zhang, M. N. Banis, J. Liu, D. Geng, R. Li, X. Sun, *J. Colloid Interface Sci.* **2012**, *369*, 123–128.
- [45] A. sadek Kadari, A. N. Ech-Chergui, S. K. Mukherjee, L. Velasco, R. K. Singh, M. walid Mohamedi, E. Akyildiz, A. Zoukel, K. Driss-Khodja, B. Amrani, M. Reda Chellali, *Inorg. Chem. Commun.* **2021**, *132*, 108852.
- [46] A. Viswanathan, A. N. Shetty, *J. Energy Storage* **2020**, *27*, 101103.
- [47] L. Manjakkal, A. Pullanchiyodan, N. Yogeswaran, E. S. Hosseini, R. Dahya, *Adv. Mater.* **2020**, *32*, 1907254.
- [48] A. Viswanathan, A. N. Shetty, *Electrochim. Acta* **2018**, *289*, 204–217.
- [49] X. Y. Liu, Y. Q. Gao, G. W. Yang, *Nanoscale* **2016**, *8*, 4227–4235.

Manuscript received: October 11, 2022

Revised manuscript received: November 15, 2022

Accepted manuscript online: November 22, 2022

Version of record online: December 5, 2022